Electromagnetic Vibrational Energy Harvesters and Power Management

by

Bassam Tunkar

A thesis
presented to the University of Waterloo
in fulfillment of the
thesis requirement for the degree of
Master of Applied Science
in
Mechanical and Mechatronics Engineering

Waterloo, Ontario, Canada, 2015

Author's Declaration

I hereby declare that I am the sole author of this thesis. This is a true copy of the thesis, including any required final revisions, as accepted by my examiners.
I understand that my thesis may be made electronically available to the public.

Abstract

The interest in scavenging various energy sources from the environment is rapidly increasing. Thanks to the advances in developing effective energy harvesters researches. Kinetic energy is a renewable source and it can be found numerously in the environment. One of the most popular class of the kinetic energy harvesters in this field is vibration energy harvesters (VEH). It is an electrical source that converts the vibrational energy into usable electrical energy to power up low-power portable or unreachable devices. The harvesting system can be self-powered as stand-alone or as alternative power source depending on the application.

In this thesis, we have studied and developed two architectures for electromagnetic VEHs: a baseline VEH and a springless VEH. We introduced and studied power management circuits consisting of a full-wave bridge rectifier and a smoothing capacitor. Moreover, electromechanical model was developed and validated by the comparison to the experimental data.

The basic electromagnetic VEH uses a mechanical mass-damper-spring oscillator to capture kinetic energy from vibrations. It has an electrical transducer using induction between a moving coil and a fixed magnets. It uses a cantilever suspension and operates at a frequency range of 57–59 Hz. We re-designed it using 80 turns coil-chip instead of 30-turns. The springless VEH works in a frequency range of 13–18 Hz. It was redesigned to carry 60 turns coil-chip. The re-design of the VEHs successfully increased the output voltage and power. The maximum power experimentally measured were 14.3 mW and 12.27 mW at optimal loads R_L of 40 Ω and 3 Ω, respectively.

The power management circuits introduced is consist of a MOSFET-based full-wave bridge rectifier and a smoothing capacitor to convert the VEH AC output waveform into a DC signal. We found that this rectifier can effectively convert the VEHs output with high voltage and power efficiencies $\geq$ 93 %. The smoothing capacitor trades-in the signal ripples for lower voltage and power efficiencies $>$ 79 %.

We identified the model parameters for the cantilever VEH, namely the natural frequency ω_n, mechanical Q_m and total Q_t quality factors, and effective average magnetic field density B. We solved the model equations numerically and analytically to find the eigenvalues, frequency response, output voltage and power. The model results agree with the obtained experimental results.

Acknowledgements

My sincere thanks and gratitude to my supervisors: Prof.Yavuz and Prof.Eihab for their guidance through my study at the University of Waterloo. I would like to thank my mentors and friends Dr. Khater and Dr. Park for their effort in giving me technical advices and support. I also would like to thank Prof. Ramahi and Prof. Fidan to be my thesis committee. My sincere gratitude to all grad students that involved in my academic career.

I dedicate the fruit of this work to all of my family, especially to my mother, wife and son for their love, care and encouragement. You always have been my motivation to work harder, Thank you!

I pray to GOD to protect all of you and wish you the best in your life.

Contents

List of Figures

List of Tables

Chapter 1

Introduction

Since the beginning of time, humanity has used various types of energy conversion to meet different needs, such as residential, commercial, transportation and industrial applications. The intensive usage of non-renewable energy can badly affect the environment and eventually human life. A trend has grown towards the use of renewable energy to reduce stress levels on the environment and living organisms. Renewable energies are environment-friendly, such as wind, water and solar energies that can be reused without harming the earth. The common method in accessing renewable energy is via energy harvesting.

1.1 Energy Harvesting

Energy harvesting is a process in which energy in the environment is captured and converted into usable electrical energy [1]. There are various types of ambient energy sources, such as wind, solar, mechanical vibrations, thermal, and radio frequency energies. The output power generated by harvesting is usually low; therefore, it is mostly deployed to low power devices, such as wireless sensors [2]. Energy harvesters can replace batteries and work as a maintenance free stand-alone power source; where as batteries have a limited life span, need periodic maintenance, have higher replacement complexity and contain hazardous materials [3]. Energy harvesters can be used in rural or dangerous areas. They can re-charge wireless sensors

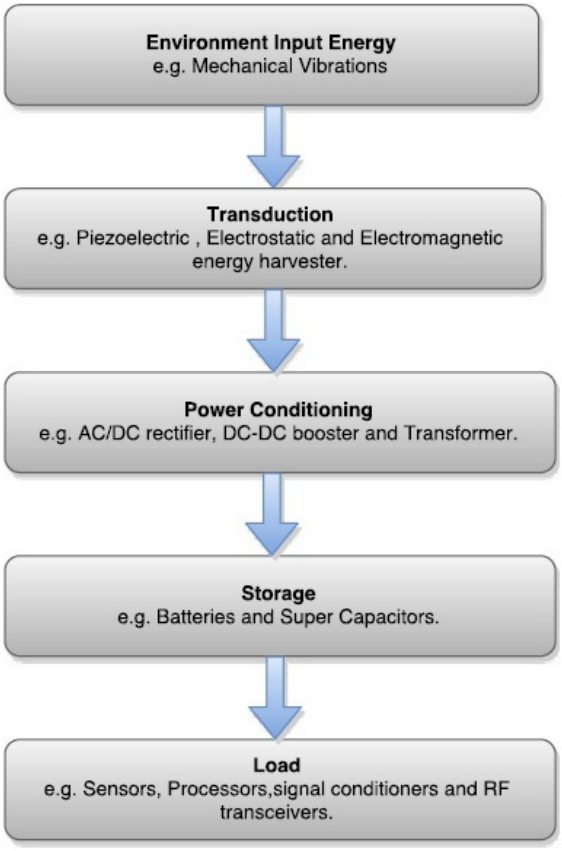

Figure 1.1: Stages of energy harvesting

continuously or discretely without human interference.

Figure 1.1 shows the stages of energy harvesting starts by capturing energy from the environment. It is then converted into electrical energy using different transduction techniques. The scavenged electrical power is rectified and voltage or current boosted using power conditioning circuits. Next,its stored in batteries or super capacitors to feed the load as needed [4].

1.1.1 Solar Energy Harvesting

Solar Energy has been utilized over the years to generate electricity. It is harvested from direct sun light or indoor light. Solar power systems can generate electric power in the range of milliwatts to megawatts, depending on the size and type. While solar power station may generate up to hundreds of megawatts; hand-held solar powered calculators and wrist watches generate tens of milliwatts. In between,

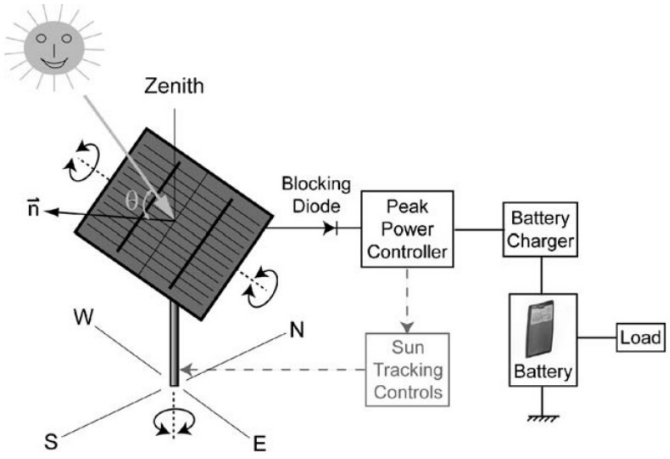

Figure 1.2: Grid-connected PV solar system [6]

small grid-connected photo-voltaic (PV) systems can generate tens of kilowatts of power to supply a small house [5].

Most of solar energy harvesters use semi-conductor photo-voltaic materials such as mono-crystalline silicon, polycrystalline silicon, and amorphous silicon. When a photon hits the solar cell, it excites electrons to jump and become free, then the electrons start to flow through the cell generating electricity, this process is called the photo-voltaic effect. A typical grid-connected PV solar system consist of a solar panel, a peak power controller, a sun tracking control unit, a battery charger and a battery as shown in Figure 1.2. It has a conversion efficiency of $\sim 15\,\%$. Sun tracking control commands the motor of the solar panel to dynamically track the sun by rotating and tilting the solar panel on two axes. The Peak power controller maintains maximum levels of voltage and current by matching the system load to the solar panel cell output [6]. Brunelli *et al* [7] present an analysis of battery-less solar circuit where they substitute the battery with super-capacitor.

1.1.2 Thermal Energy Harvesting

Thermal energy is one of the most prevalent energy sources in the environment. Thermal energy harvester is based on seebeck phenomenon [9], where the typical thermal energy harvester consists of two junctions (hot and cold) between two dissimilar materials (metals or semiconductors), and a circuit connecting the two

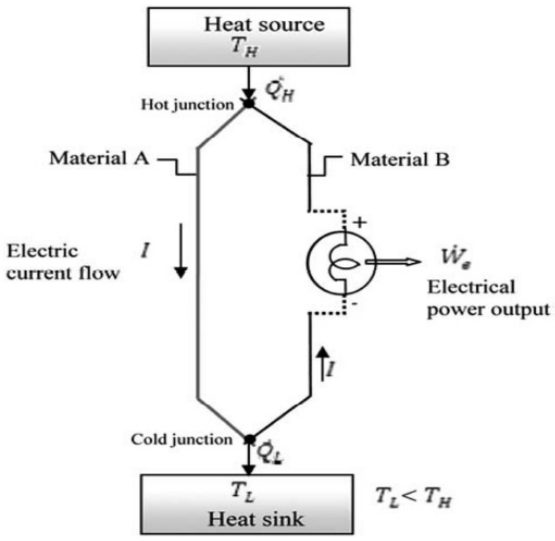

Figure 1.3: A typical thermoelectric generator [8]

junctions as shown in Figure 1.3. When expose to heat, the temperature difference between the hot and cold junctions creates a potential voltage, where the energy conversion efficiency is $\sim 5\,\%$ [10].

1.1.3 Radio Frequency Energy Harvesting

With the development of wireless telecommunication technologies (e.g. GSM, Wi-Fi, Bluetooth and WLAN) ambient radio frequency power became an attractive source for energy harvesting. A typical RF energy harvester, called a rectified antenna "rectenna" [11], converts microwave energy into DC signal. The rectified antenna consists of an antenna, microwave low-pass filter (MLPF), rectifier circuit, DC filter and load as shown in Figure 1.4. When the antenna receives microwave signals, it functions as a band bass filter, where it only capture the resonant frequency of the antenna. Next, the low-pass filter suppresses higher order harmonics to increase conversion efficiency and to matches the impedance of the antenna to the impedance of the rectifier. The rectification circuit converts the AC signal into DC signal. However, some AC components are not totally converted into DC; therefore, a DC filter open circuits the remnant of alternate current and passes only direct current to the load.

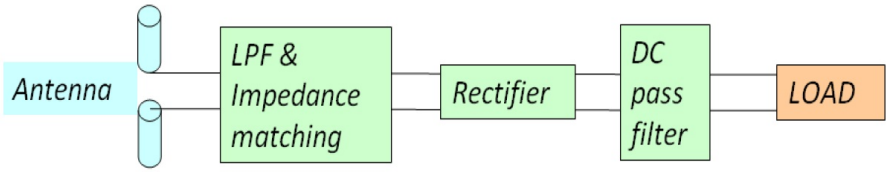

Figure 1.4: Block diagram of the rectenna [11]

There are many types of ″rectennas‶such as the dipole rectenna, patch rectenna, spiral rectenna and slot rectenna. Some rectennas designed for narrow band operation in a frequency range of $\sim 2.5\,\mathrm{GHz}$, while others are designed for wide band operation in a frequency range of 1.7–2.5 GHz. Both designs can achieve high conversion efficiencies over 60 % [12].

1.1.4 Kinetic Energy Harvesting

Kinetic energy is energy stored in moving objects, representing the work done to accelerate the object from rest. This kind of energy is found in the environment in many forms as vibrations, rotational kinetic energy and translational kinetic energy. It is present in the movement of living beings and machines, acoustics vibrations, natural events as earthquakes, mechanical impacts of bodies and sea waves. It can be converted into other useful forms such as potential, heat, sound and electrical energy. Different transduction techniques have been used to scavenge kinetic energy from the environment and convert it into electrical energy.

1.2 Vibration Energy Harvesting

This thesis focuses on vibration energy harvesters and their power management circuits. This section will discuss the principles of vibration energy harvester and review the state-of-art of the harvesting techniques.

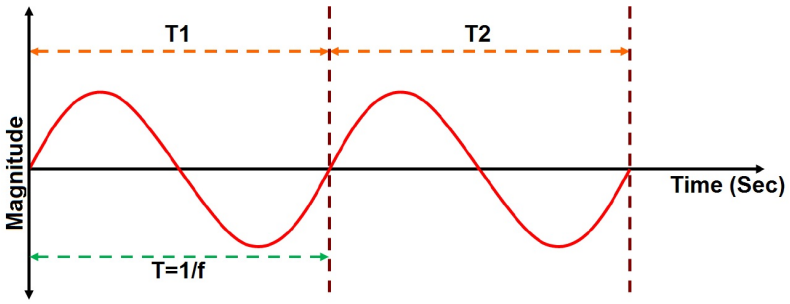

Figure 1.5: Periodic vibration motion

1.2.1 Vibration Energy Harvesting

Vibrations are periodic motions of a body. This motion repeats itself at a characteristic time interval T as shown in Figure 1.5, with an amplitude A and a frequency Ω. It can be described as:

$$x(t) = A\ cos(\Omega t) \tag{1.1}$$

where $x(t)$ is the displacement of the body as a function of time t. The equation of motion of a base excited linear oscillator can be written as:

$$m\ddot{x} + c\dot{x} + kx = -m\ddot{y} \tag{1.2}$$

where $x(t)$ is the relative displacement of the oscillator. The oscillator, Figure 1.6, is made of a traveling mass m, a spring k and a damper c moving in response to base displacement $y(t)$. The undamped natural frequency of the oscillator is

$$\omega_n = \sqrt{\frac{k}{m}} \tag{1.3}$$

When the frequency of base excitation matches the natural frequency of the harvesting oscillator $\Omega = \omega_n$, the energy harvester extracts peak power from the environment [13]. Damping for a harvesting oscillator lumps mechanical and electrical energy losses $c = c_m + c_e$. There are three main types of frequency responses when a system oscillates due to motions:

- **Undamped response:** when energy losses are ignored.

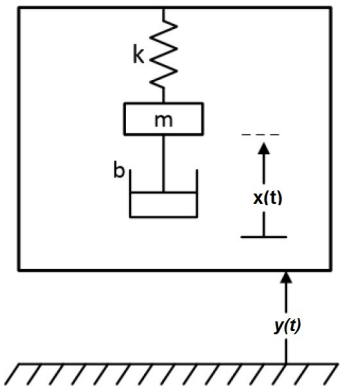

Figure 1.6: Mass-spring-damper oscillator [14]

- **Over-damped response:** when the system response exponential decays to equilibrium without oscillation.
- **Under-damped response:** when the system response decays to zero with oscillation.

1.2.2 Electrostatic Harvesters

The main concept of electrostatic harvesters is to convert vibrations into variable capacitive charge between two plates, which flows as a current to feed the load. The capacitive charge can be increased or decreased by changing the distance between the capacitor plates or each plate surface area [15].

A state of the art electrostatic MEMS power generator was presented by Tao *et al* [16]. This generator is made of three parallel silicon plates. The middle plate is a movable plate carries double sided electrodes. There is a 180° phase difference between the bottom and middle as seen in Figure 1.7.

When external forces are applied to it, the variation in capacitance between the plate electrodes (top and bottom electrodes) creates current flow. The harvester operates at 125 Hz harvesting an overall power of 0.12 μW at an acceleration of 0.2 g.

A two degree of freedom MEMS electrostatic energy harvester has also been developed by Tao *et al* [17]. The device is based on a movable disc electrode sus-

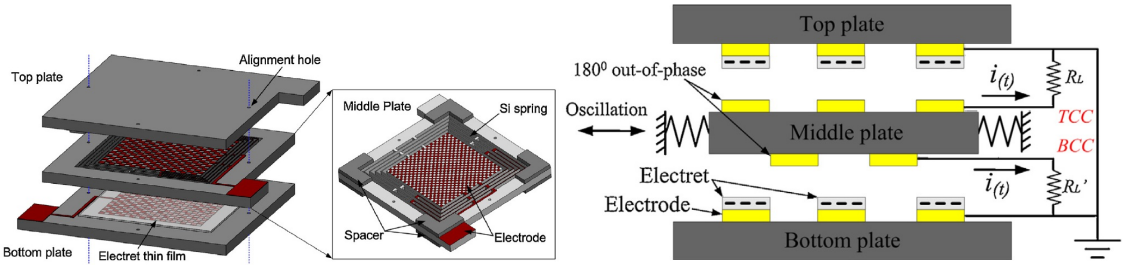

(a) 3-D view (b) Cross sectional View

Figure 1.7: Sandwich structured electromagnetic energy harvester [16]

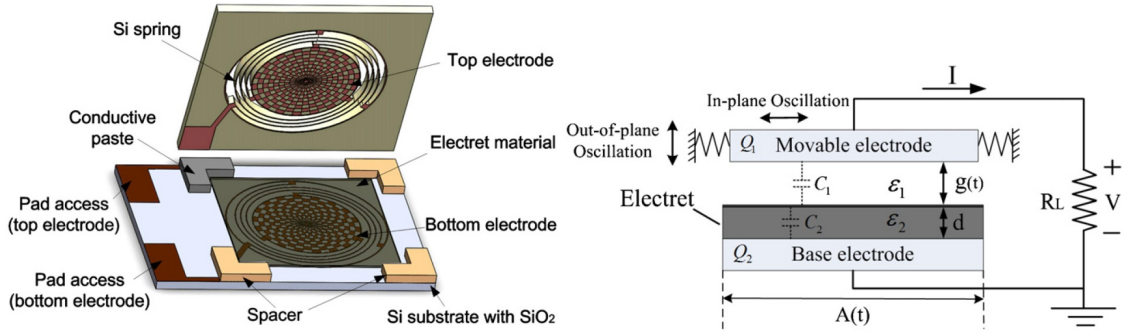

(a) 3-D view (b) Cross sectional View

Figure 1.8: Disc structured electromagnetic harvester [17]

pended by a spiral spring and a fixed bottom electrode. Force is applied to the disc in two different configurations, the first one is out-plan where the disc moves vertically, and the space between the electrodes change. The second configuration is in-plan where the disc moves horizontally and causing overlap between electrodes as shown in Figure 1.8. The harvester operates between 66–78.5 Hz in three vibration modes depending on the direction of the disc. The harvester results show a maximum power output of 4.8 nW at 0.05 g.

A low frequency electrostatic harvester working at 2 Hz was introduced by Naruse *et al* [18]. The harvester consists of an electret plate on a middle silicon substrate,two top and bottom collector electrodes on glass substrates and micro ball bearings among the three substrates. The harvester collects charges when the electret is aligned with a first collector electrode. As the electret transits from the collector electrode (1) to the collector electrode (2) due to oscillation, the charges transfer through the load connected between the two collector electrodes as shown

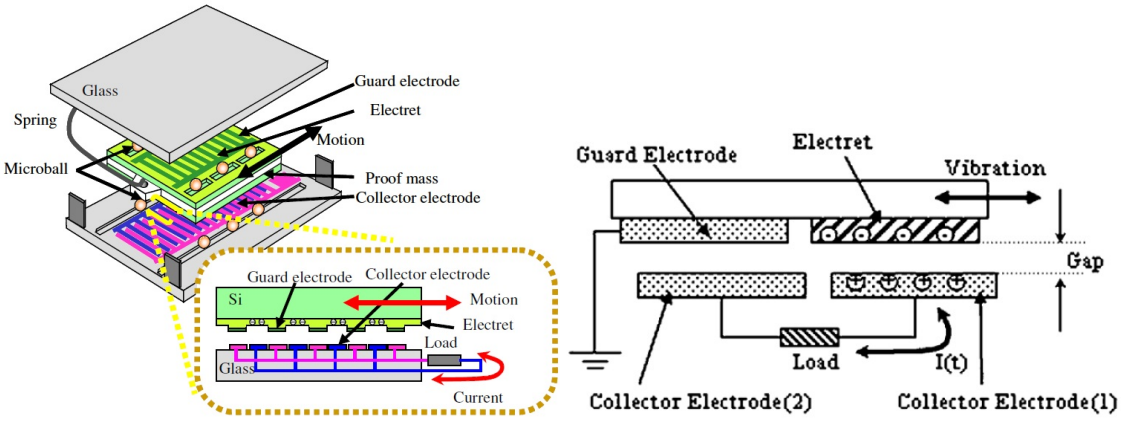

(a) 3-D view (b) Cross sectional View

Figure 1.9: Human motion electrostatic harvester [18]

in Figure 1.9. This harvester demonstrated maximum output power of 40 μW at 0.4 g when connected to 7 MΩ load resistance.

Electrostatic technique is a preferable candidate of MEMS energy harvesting, because of its CMOS compatibility and micro-fabrication process ease [19]. On the other hand, their low current output due to its high output impedance and their dependence on external voltage source [20] make the use of electrostatic technique in an ongoing challenge.

1.2.3 Piezoelectric Harvesters

Piezoelectric materials develop a potential difference when deformed under applied stress [21]. There are many types of piezoelectric materials including polyvinylidene fluoride (PVDF) and lead zirconate titanate (PZT). Piezoelectric harvesters can be implanted inside the human body to act as human based energy generators [22]. Dagdeviren *et al* [23] used animal models to approximate human size organs to demonstrate theses generators. They developed a thin film device made of PZT ribbons and two electrodes fabricated on top and bottom of the film. An interconnection array was implemented 10 PZT ribbons connected in parallel to increase output current and 12 sets of PZT ribbons connected in series to increase output voltage, Figure 1.10. The results show that the peak voltage and current at maximum contraction is 3.7 V and 0.15 μA, respectively.

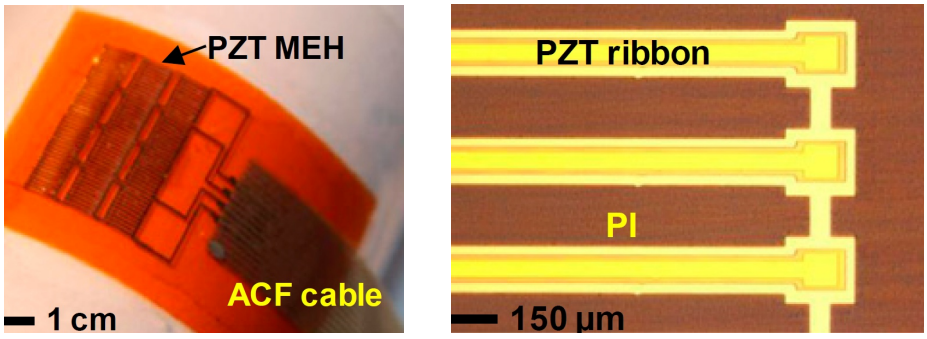

(a) Full PZT array (b) PZT ribbons connected in parallel

Figure 1.10: Implant piezoelectric energy harvester [23]

Another piezoelectric human based energy generator is designed to be installed in shoes sole to convert the bending movement of the foot into electrical energy [24]. Results show that at a gait frequency of 0.9 Hz, the maximum output power is 1.3 mW when connected to a resistive load of 250 kΩ.

A typical structure of piezoelectric harvester is a simple fixed-free cantilever beam with the piezo material mounted at the beam root. The beam consists of a mass placed at the middle or the end. The location of the proof mass changes the damping and natural frequency of the system; the farther the mass the higher the damping and lower natural frequency. A low frequency piezo cantilever beam energy harvester was presented by Han and Yun [25] using snap-through-buckling to harvest low acceleration beams vibrations. The device consists of two elastic sidewall beams with a buckled bridge beam connected between them, Figure 1.11. Two piezoelectric cantilever beams and a proof mass are placed on the top of the bridge beam. The maximum output power of this device was 10 μW at excitation frequency of 15 Hz and acceleration amplitude of 0.5 g.

Piezoelectric harvesters can produce a high voltage output compared to electrostatic and electromagnetic energy harvesters. Furthermore, they are compatible with MEMS due to their miniaturize dimensions. However, they have low current (nA–μA) and high output impedance (on order of 100 kΩ).

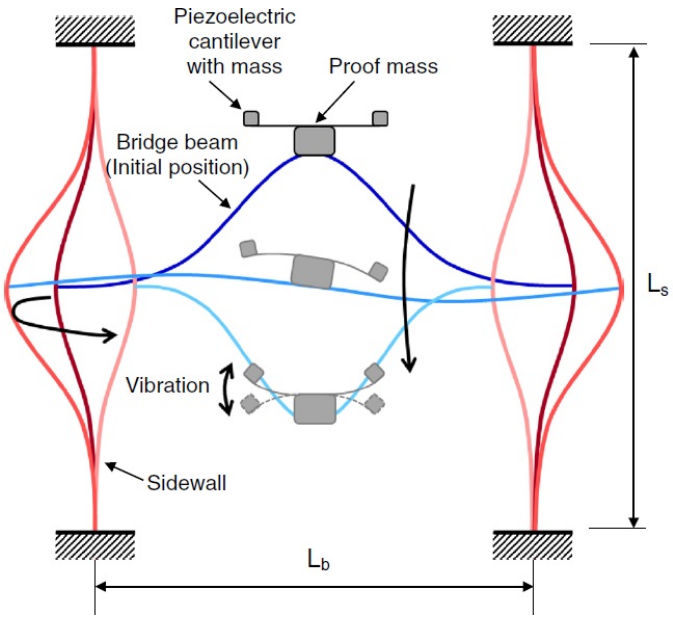

Figure 1.11: Novel cantilever based piezoelectric energy harvester [25]

1.2.4 Electromagnetic Harvesters

Electromagnetic energy harvesters are based on electromagnetic induction. This phenomenon is described by Faraday's law, which explains the interaction of magnetic flux with conductive coil. Faraday's law states that any change in the magnetic flux will cause an electromotive force (EMF) in the coil. The voltage generated (V) is proportional to the rate of change of the magnetic flux ϕ_m and the number of coil turns N:

$$V = -N\frac{d\phi_m}{dt} \tag{1.4}$$

The induced output voltage of electromagnetic energy harvesters is relatively small. Therefore, different methods had been developed to amplify the output voltage; such as increasing the number of turns of the coil N or increasing the change in the magnetic flux ϕ_m, for example using stronger magnets. The relative motion between the coil and magnet(s) cause a relative displacement $\frac{dx}{dt}$ in the direction x and results in the creation of potential difference in the coil that can be expressed as:

$$V = -N\frac{d\phi_m}{dt}\frac{dx}{dx} \tag{1.5}$$

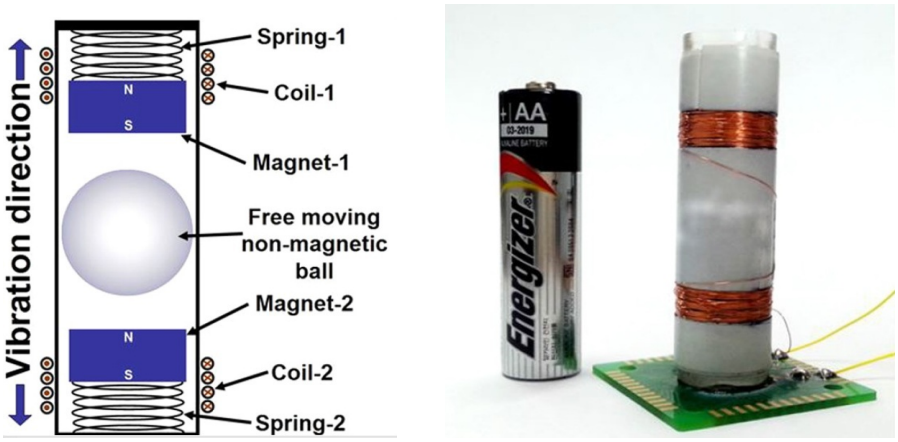

(a) Schematic diagram (b) Actual device

Figure 1.12: Tube electromagnetic energy harvester [26]

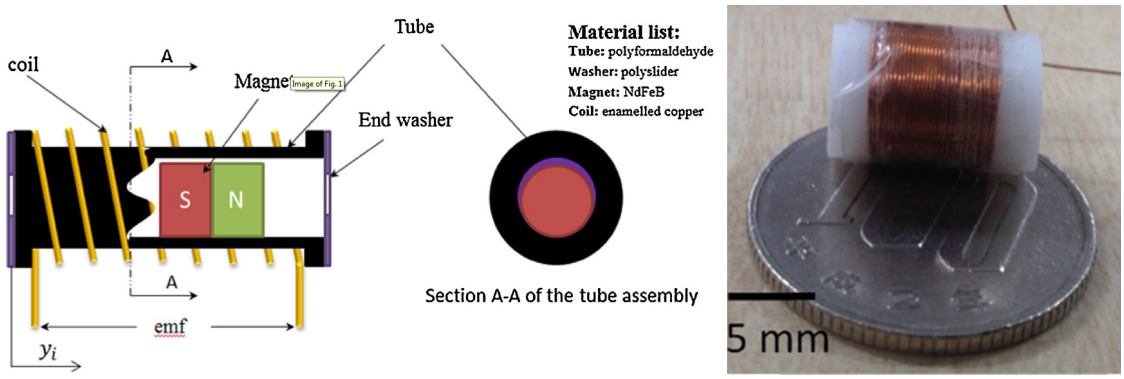

(a) Schematic diagram (b) Actual device

Figure 1.13: Tube electromagnetic energy harvester [27]

Halim *et al* [26] presented an electromagnetic energy harvester that operates in low frequency ($< 5\,\text{Hz}$). The harvester consists of a non-magnetic steel ball inside a cylindrical tube, two springs, and two magnets. The ball moves freely when excited inside the tube striking the end magnets as shown in Figure 1.12. Two different methods were used to test the harvester, a shaker and a manual hand shake. The results show that the average power generated by hand shaking is $110\,\mu\text{W}$.

Another state of the art electromagnetic low frequency energy harvester has been developed by Haroun *et al* [27] for frequencies in range of 2.5–3.33 Hz. The harvester includes a free magnet inside a tube and stoppers at the ends of the tube to create an impact, Figure 1.13. Different tube dimensions and magnet shapes

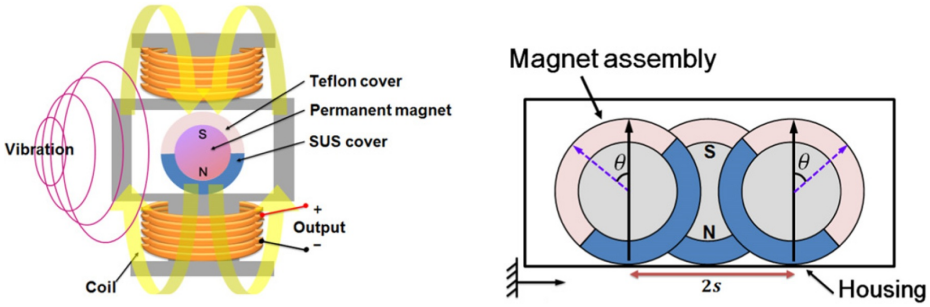

(a) Schematic diagram (b) Magnet sway motion

Figure 1.14: Roly-poly electromagnetic harvester [28]

were tested to optimize power. The highest output power this device can harvest is 113.3 μW at 3.33 Hz and 71.8 μW at 2.5 Hz.

Choi *et al* [28] developed an approach to magnet and coil interaction. A springless spherical magnet has been designed such that the center mass was away from the sphere center.The ball sways when external forces are applied while maintaining an upright position as shown in Figure 1.14]. This energy harvester has a maximum output power of 9.03 μW at 20 Hz acceleration with amplitude of 3 g connected to 80 Ω load.

Our aim in this thesis is to study and optimize two architectures of electromagnetic energy harvesters. We will provide experimental results that surpass the electromagnetic literature review in terms of voltage and power.

1.3 Power Conditioning

The limited output power from harvesters require the design of lower dissipation and higher efficiency power conditioning circuits. Moreover, the harvester impedance, and therefore level of output voltage and current, depends on its transduction mechanism. For example, piezoelectric harvesters have relatively high impedance output ($\leq$ 100 KΩ) resulting in high voltage ($\geq$ 1 V) and low current output (on the order of μA). On the other hand, electromagnetic harvesters have low impedance (in Ohms) resulting in low out put voltage (on the order of mV) and current on the order of mA.

Power conditioning circuits can be classified in three categories:

- Voltage or current boosters, such as DC-DC boosters, voltage multipliers and Maximum Power Transfer Tracking (MPTT) circuits [29].
- AC/DC converters, such as full-wave, half-wave rectifiers, passive and active rectifiers, and ripple smoothing circuits [30].
- Voltage stabilizers/regulators.

In this thesis, the focus is on AC/DC conversion, thus, more details will be provided on this category only.

1.3.1 AC/DC Converters

Vibration based energy harvesters alternating current (AC); thereby requiring a AC/DC conversion to power up electronics devices that utilize DC power supply. The most common converters are bridge(full-wave)rectifiers, center tap rectifiers and half-wave rectifiers. Passive rectifiers do not require external power supply, in addition to the energy harvester. On the other hand, active rectifiers require extra circuitry and an additional power supply, which adds to cost, complexity and size of the power unit.

1.3.1.1 Components

AC/DC rectification circuits utilize basic components, such as diodes, transformers, capacitors and MOSFETs. Diodes are one of the fundamental nonlinear components which has nonlinear $[i - v]$ characteristics. Diodes operate in two different modes, a forward biased mode and a reverse biased mode. In forward bias mode, the diode allows current to flow, and in reverse bias mode, it blocks current passage. Ideal diodes allow current to pass through in one direction only, while totally blocking reverse direction, means that output voltage should be the same as input voltage $V_{out} = V_{in}$. In practice, diodes have leakage current flow in the opposite direction in reverse biased mode; in addition to a forward voltage drop needed to

pass the current resulting in $V_{out} \cong V_{in} - V_d$, where V_d is the diode forward voltage drop [31]. Each diode have a different V_d, as shown in Table 1.1.

Table 1.1: Forward voltage drop V_d for various diodes

Diode Type	**Voltage Drop**
Silicon	0.7 V
Germanium	0.3 V
Schottky	0.2 V

Since electromagnetic energy harvesters have a typically low output voltage; diodes voltage drop V_d stops current passage, and therefore energy harvesting during the part of the harvesting cycle where $V_{in} < V_d$ and at $V_{in} > V_d$ the diodes start to conduct current, therefore the energy harvesting will provide a DC power. This make Schottky diodes popular due to its lower forward voltage drop.

While, transformers are popular components in rectification circuits, in low-power energy harvesting they are not efficient because of the high power losses via Hysteresis losses, Joule losses and flux leakage. Ideal transformers neglect all theses losses and convert AC voltage from one level to another level.

$$\frac{V_p}{V_s} = \frac{I_s}{I_p} = \frac{N_p}{N_s} = a \tag{1.6}$$

where V_p and V_s are the voltage on the primary and secondary windings, respectively, I_s and I_p are the current of the primary and secondary windings, respectively, N_p and N_s are the primary and secondary coil number of turns, respectively, and a is the turns ratio.

Capacitors store electrical energy in a process called charging, and release it in a process called discharging. The capacitor consists of two 'plates' and a non-conductive layer between them. The capacitance can be expressed as

$$C = \frac{\epsilon_r \epsilon_0 A}{d} \tag{1.7}$$

where A is the plate area, d is the distance between the plates, ϵ_0 is the permittivity

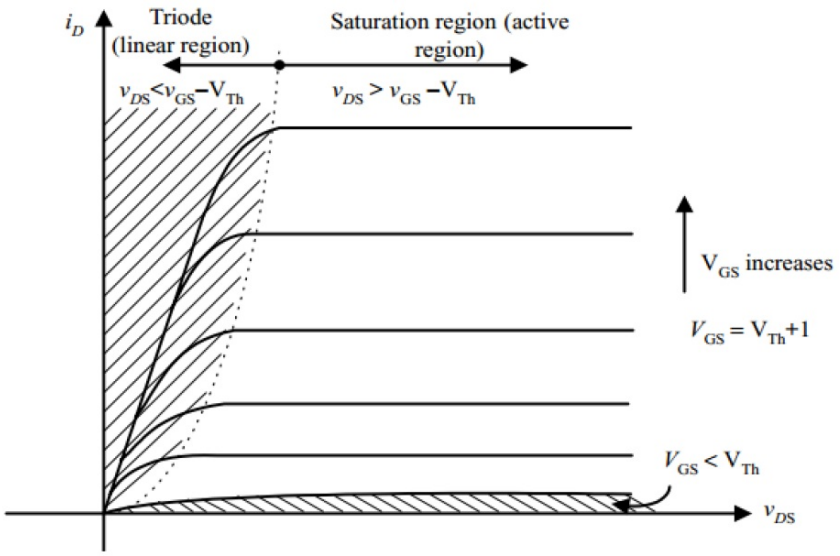

Figure 1.15: MOSFETs $i - v$ characteristics [32]

of free space and ϵ_r is the relative permittivity of the dielectric material between the plates. Capacitors play an important role in smoothing output ripples after the rectification and as a storage element after the power conditioning.

MOSFETs (Metal Oxide Semiconductor Field Effect Transistors) are another alternative to diodes. MOSFETs are active, voltage controllable, devices where the source-to-drain current I_{ds} can be controlled by the gate-to-source voltage V_{gs}. MOSFETs operate in three different regions as illustrated by the $i-v$ characteristic curves shown in Figure 1.15: a cut-off region, a triode(linear) region, and a saturation region. The cut-off region is when the gate-to-source voltage V_{gs} is less than the threshold voltage needed to create a conduction path between the drain and source $V_{gs} < V_{th}$, no current pases from the source-to-drain I_{ds} in this case. The triode region occurs where the voltage between the drain and source is less than gate-to-source voltage minus the threshold voltage $V_{ds} < V_{gs} - V_{th}$. The last region is the saturation region where the conduction path is fully opened and the voltage between the drain and source is larger or equal to the gate-to-source voltage minus threshold voltage $V_{ds} \geqslant V_{gs} - V_{th}$. In electromagnetic harvesting, the MOSFETs mostly operate in the linear and cut- off regions only because of the low voltage level provided by the harvester.

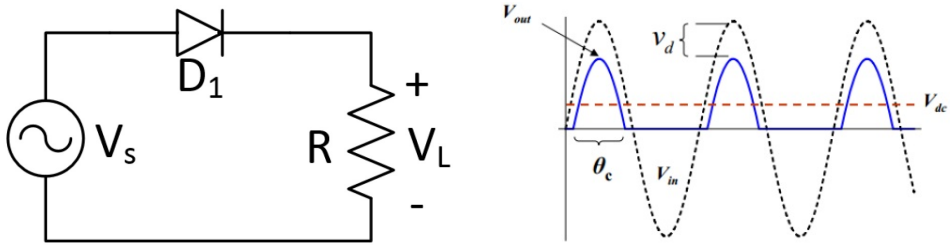

(a) Half-wave rectifier circuit diagram (b) Actual have-wave rectifier output

Figure 1.16: Half-wave rectifier circuit [33]

1.3.1.2 Half-Wave and Full-Wave Rectification

Half-wave rectifiers pass only half of the sinusoidal input cycle and eliminate the other half, as a result 50 % of the output power eliminated. Half-wave rectifiers consist of only one diode and a load as shown in Figure 1.16a. Half-wave rectification is not perfect for energy harvesting applications as shown in Figure 1.16b. The average dc output voltage of a cycle period T can be calculated as,

$$V_{dc} = \frac{1}{T}\int_0^T V(t)dt = \frac{V_{in}}{\pi} \tag{1.8}$$

Full-wave rectifiers pass both positive and negative sides of the input signal. Their advantages over half-wave rectifiers are larger average *dc* output voltage and power and lower ripples. Typical center tap rectifiers contain a transformer and two diodes, Figure 1.17. Each diode and half side of the transformer rectify a half-wave cycle. Bridge rectifiers contain four diodes, two diodes configured to work in each half-cycle only [34].

Center tap rectifiers are less efficient than bridge rectifiers because of the use of a transformer that reduces power efficiency and increases rectifier size and total cost. As a result, bridge rectifiers are more suitable for low power systems.

1.3.1.3 Active and Passive Rectification

Active rectification seeks to improve the power efficiency of rectification circuits using active switches, such as MOSFETs or power Bipolar Junction Transistors

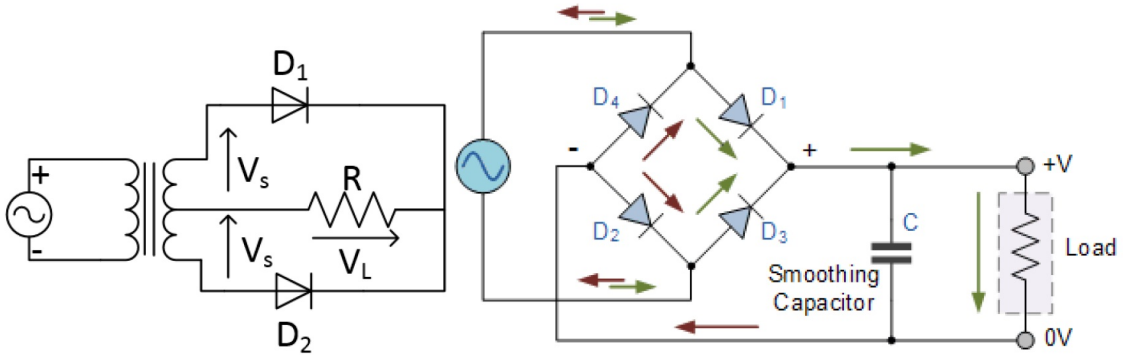

(a) Center tap rectifier (b) Full-wave bridge rectifier

Figure 1.17: Typical full-wave rectifier [35]

(BJTs), and control them by an external DC power supply. Passive rectification circuits typically consist of diodes and do not require external power supply. The use of active MOSFETs over the passive diodes have a very low internal resistance advantage R_{ON} as low as $m\Omega$ compared to diodes. The voltage drop across MOSFETs $V_{ds} = I_{ds}R_{ON}$ is much lower than diodes which reduces power loss and increases power efficiency. In comparison, the voltage drop in full bridge rectifiers is doubled because two diodes works as pair in each half-cycle $V_{out} \cong V_{in} - 2V_d$.

1.4 Motivation

The thesis motivation is to improve the efficiency of electromagnetic energy harvesting. There are many mechanical factors that can help in increasing the output power such as harvester structure and size and weight of the seismic mass. The mechanical structure affect on the maximum output power, nonlinearity and natural frequencies of the system. Decreasing the harvester size to micro level make it more deployable almost every where, however it also minimize the output power drastically. The power conditioning circuits can dissipate most of the acquired power and drastically reduce the overall system efficiency. Thus high efficiency power conditioning circuits, less electronics usage and lower mechanical damping are all important steps toward optimal energy harvesting.

1.5 Thesis Outline

This thesis arranged in a total of five chapters. Starts with chapter one, we demonstrate different types of energies and their energy harvesting applications. Then, we particularly explained the vibration energy harvesters (VEHs) and their transducer techniques. A literature review introduced in this chapter listing the state-of-art of some VEH transduction techniques. Next, we demonstrate different power conditioning circuits and their components specially the rectification circuits.

In chapter two, we introduce a cantilever vibration energy harvester (VEH) and its power conditioning circuits. The VEH tested with different coil turns where the VEH re-designed to carry 80 coil turns instead of 30 turns. Three stages introduced to analyze the VEH performance with a full-wave bridge rectifier and smoothing capacitors. Analysis techniques implemented to compare the VEH parameter alterations and output voltage and power with different coil turns.

In chapter three, Parameter identification techniques used to obtain some parameters using the experimental data of chapter two. We lumped model the mechanical and transduction parts of the VEH and couple them with coupling forces. The mechanical and electrical coupled models are solved homogeneously and particularly to find the eigenvalues and output voltage and power.

In chapter four, we introduce another energy harvester architecture which is the springless vibration energy harvester (SVEH). The SVEH re-designed to hold 60 coil turns instead of 40 turns, then tested with the full-wave bridge rectification circuit. We apply different analysis techniques to study the performance of the SVEH such as output voltage and power.

Chapter 2

Cantilever Electromagnetic VEH

2.1 Introduction

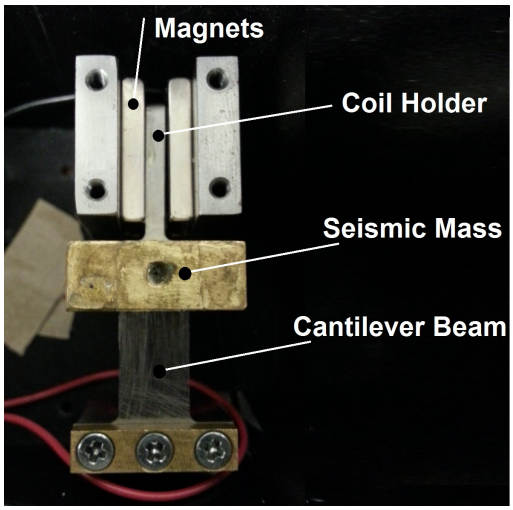

Figure 2.1: Top-view of VEH

Electromagnetic vibrational energy harvesters (VEH) couple a mechanical oscillator to an electromagnetic transducer. The oscillator, Figure 2.1, is made of a cantilever beam, a seismic mass m, and damper with a damping coefficient of c. When the base moves with a harmonic motion $y(t)$ at a frequency Ω, the cantilever beam and the proof mass move with respect to the base by a relative displacement

$x(t)$. Using Newton's second law, we write the oscillator's equation of motion as:

$$m\ddot{x} + c\dot{x} + kx = -m\ddot{y} \tag{2.1}$$

dividing Equation (2.1) by mass (m) we got:

$$\begin{aligned} -\ddot{y} &= \ddot{x} + 2\zeta\omega_n\dot{x} + \frac{k}{m}x \\ \ddot{x} &= -\frac{\omega_n}{Q}\dot{x} - \omega_n^2 x - \ddot{y} \end{aligned} \tag{2.2}$$

The cantilever beam stiffness, resistance of motion, can be calculated as

$$k = \frac{3EI}{L^3} \tag{2.3}$$

where E is the material elastic Young's modulus, I is the cross section second moment of area, and L is the cantilever length.

Assuming a linear oscillator under a sinusoidal base excitation, the steady state solution of Equation (1.1) can be written as [36]:

$$x(t) = \frac{1}{\sqrt{(\frac{k}{m} - \Omega^2)^2 + (\frac{c\Omega}{m})^2}} A_\circ \sin(\Omega t + \phi) \tag{2.4}$$

where $A_\circ$ is the amplitude of base acceleration. The average input kinetic energy E_{Avg} is obtained from the average velocity of the mass v_{Avg} over a period as:

$$E_{Avg} = \frac{1}{2} m v_{Avg}^2 \tag{2.5}$$

Likewise, the average power flow from the base to the harvester [37] can be calculated as:

$$P_{in} = \frac{2\pi E_{Avg}}{\Omega} = \frac{\pi m}{\Omega} v_{Avg}^2 \tag{2.6}$$

and also can be describe as:

$$P_{in} = \frac{1}{2} A^2 Q_t \omega_n m \tag{2.7}$$

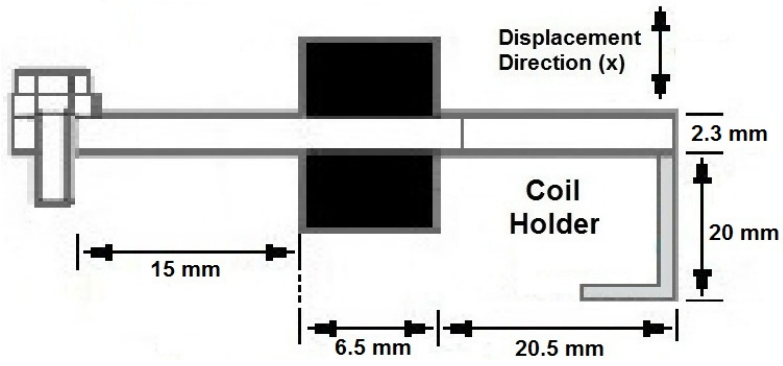

Figure 2.2: Schematic side-view of the VEH

The electromagnetic transducer consists of a magnetic circuit and a coil. The coil and mass are attached to the moving cantilever beam but the magnets are fixed to steel cage. Individual magnets are arranged into a magnetic circuit to insure that the highest magnetic flux density B cross the coil turns. The electrical side of the VEH dissipates some of the kinetic energy in the coil R_c and load R_L resistances, these losses are denoted as electrical damping. The electrical damping force [38] can be describe as

$$c_e\dot{x} = B\ell I \tag{2.8}$$

$$c_e\dot{x} = B\ell\frac{V}{R_L + R_c} = B\ell\frac{B\ell\dot{x}}{R_L + R_c} = \frac{(B\ell)^2\dot{x}}{R_L + R_c} \tag{2.9}$$

where B is the magnetic flux density, V is the total voltage generated in the coil, and ℓ is the effective coil length.

The other source of energy dissipation in the harvester is mechanical losses represented by a viscous damping coefficient c_m such as friction and parasitic damping. Inserting the electrical and mechanical damping into the EoM 2.1, we obtain

$$m\ddot{x} + (c_m + c_e)\dot{x} + kx = -m\ddot{y} \tag{2.10}$$

2.2 VEH Specifications

The suspension cantilever beam and coil holder, Figure 2.2, are made from non-magnetic 316 stainless steel. The cantilever beam is 42 mm long divided into 3

sections: a coil holder (20.5 mm), a proof mass (6.5 mm), and a cantilever root (15 mm). The thickness of the cantilever beam is 2.3 mm. The seismic mass is 18 grams of brass.

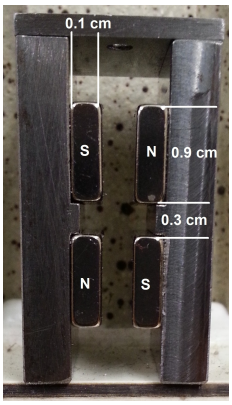

(a) Front view

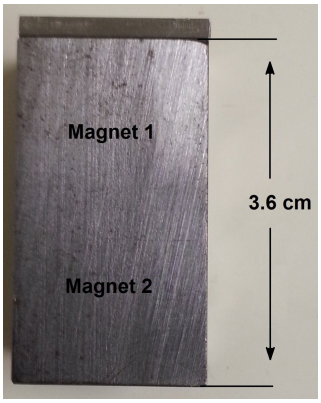

(b) Side view

(c) 3D view

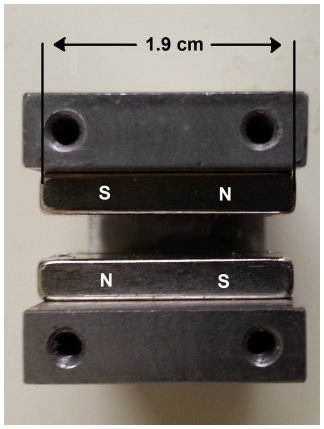

(d) Top view

Figure 2.3: Magnets and walls

A hand-made coil chip consists of two thin polycarbonate sheets and a thick square core polycarbonate sheet assembled using epoxy glue. The coil is 30 turns of hand wound magnetic wire (34 AWG). The coil core dimensions are $14 \times 11 \times 1.2$ mm and the total wire length is calculated using the equation

$$\ell_{total} = (\ell_{core} + W_{core})\ 2\ N \tag{2.11}$$

as 1500 mm. The coil chip specifications are listed in Table 2.1.

Table 2.1: Hand-made coil specifications

Coil specifications	
Type	34 AWG
Length	1500 mm
Resistance	2.2 Ω
Chip specifications	
Material	polycarbonate
Core Dimensions	$14 \times 11 \times 1.2$ mm
Outer Dimensions	$19 \times 16 \times 2$ mm

Four NdFeB Magnets are distributed along the walls of a metal cage with an air gap of 3.3 mm between the facing magnets to form a magnetic circuit, Figure 2.3. Each wall carries two magnets with a middle spacer to align the magnets with the coil lines, Figure 2.3a. The magnet poles are arranged in opposite directions S-N and N-S to create a closed magnetic circuit [39]. The dimensions of the magnet are $19 \times 9 \times 1$ mm. The cage is attached at a steel housing.

Table 2.2: Measured magnetic flux density

Sensor location	**B (G)**
a	7650
b	882
c	8167
d	253

The magnetic flux density was measured at four points along the air gap length, points (a), (b), (c), and (d) shown in Figure 2.4. The results are listed in Table 2.2. The maximum magnetic flux measured was ~ 8167 G at the center of the two lower magnets where the coil lines are located. The gauss meter used is GM-2 [40] with a minimum resolution of 0.01 G.

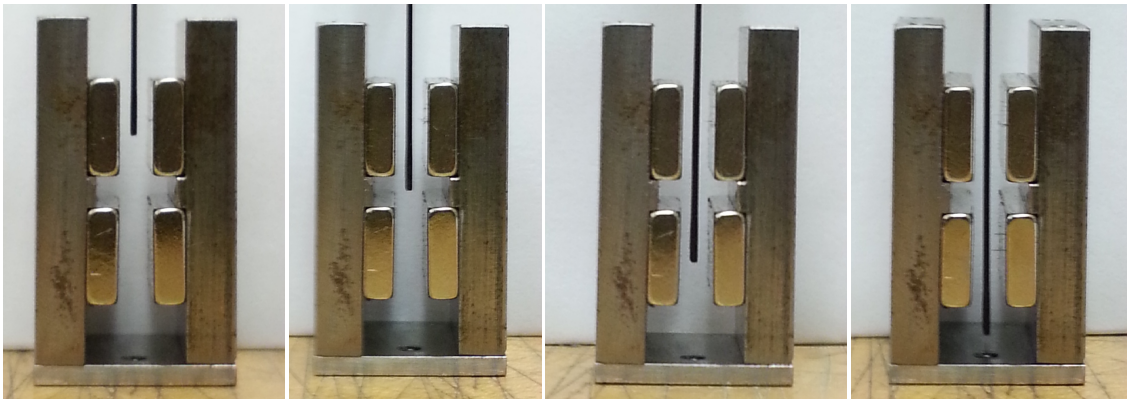

(a) (b) (c) (d)

Figure 2.4: Measuring magnetic flux density

2.3 Harvester Re-Design

The average electrical output power can be calculated as

$$P_e = \frac{\zeta_e}{4(\zeta_e + \zeta_m)^2} A_\circ^2 \omega_n m \tag{2.12}$$

where ζ_e and ζ_m are the electrical and mechanical damping ratios. The electrical damping ratio can be derived from Equation (2.9) as

$$\zeta_e = \frac{(B\ell)^2}{2m\omega_n\big(R_L + R_C\big)} \tag{2.13}$$

Using Equation (2.13) in Equation (2.12), we obtain

$$P_e = \frac{B^2\ell^2 A_\circ^2}{8(R_L + R_C)(\zeta_e + \zeta_m)^2} \tag{2.14}$$

We can use the relationship between the quality factor and the total damping ratio ($Q_t = 1/2\zeta_t$) to rewrite the average output power as

$$P_e = \frac{B^2\ell^2 A^2 Q_t^2}{2(R_L + R_C)} \tag{2.15}$$

From Equation (2.15), we conclude that the options to increase the harvester

output power are: increasing the magnetic flux density B, the effective coil length ℓ, or the harvester total quality factor Q_t. The relative merits of each of these options are:

- Using stronger (thicker) magnets will increase the magnetic flux density B, however increasing the magnets dimensions will significantly increase the size and weight of the VEH and make the overall system bulkier.

- Decreasing the air gap in the magnetic circuit will increase the magnetic flux B on the coil but require decreasing the thickness of the coil chip and lead to a lower number of coil turns. In addition to, the will increase the likelihood of coil-magnet friction, thereby lower the quality factor, and make coil alignment inside the magnetic circuit significantly harder.

- Decreasing the total damping of the harvester is an attractive route. However, in the current VEH design there are no obvious options to reduce mechanical damping beyond elimination of coil-magnet friction and backlash in the cantilever beam support.

- Increasing coil number of turns will increase the Electromotive force (EMF) induced in the coil and without requiring significant structural modifications.

Therefore, increasing the number of turns is a better option to optimize harvester. This is specially true since there is enough space to design a new coil chip that can house a higher number of turns without leading to coil-magnet friction.

A cheap and accurate way to fabricate the coil chip is 3D printing. A new coil chip was made from polycarbonate-acrylonitrile butane styrene (PC-ABS) using enhanced 3D printing with a dimensional tolerance of $\pm 127\,\mu$m [41]. The dimensions are designed to better locate the coil lines at the centers of the top and bottom pairs of magnets where maximum flux density is located. The size of the core was reduced to allow for a larger number of coil turns. The dimensions of the coil chip are listed in Table 2.3 and the blue print of the new coil is shown in Figure A1. The new chip can carry up to 80 coil turns equivalent to 3360 mm coil length.

Table 2.3: 3D coil-chip specifications

Coil specifications	
Type	34 AWG
Length	3360 mm
Resistance	4.2 Ω
Inductance	125 μH
Chip specifications	
Material	PC-ABS
Core Dimensions	11 × 10 × 1.2 mm
Outer Dimensions	18 × 17 × 2 mm

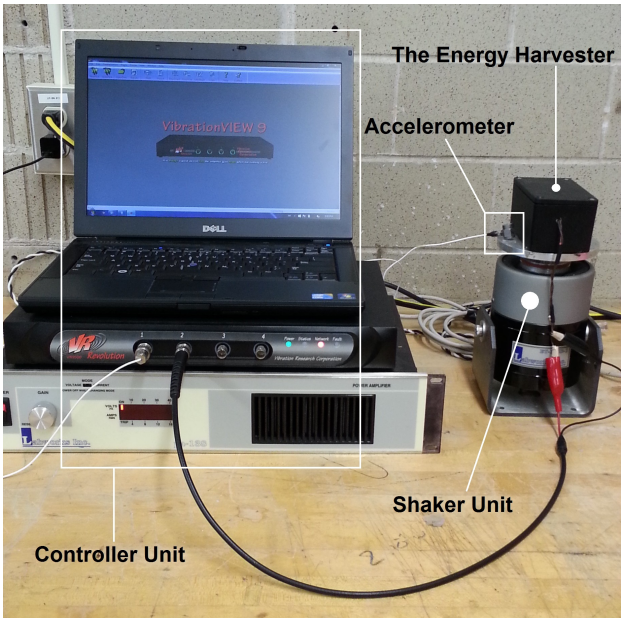

Figure 2.5: VEH Experimental setup

2.4 Experimental Setup

The experimental setup, shown in Figure 2.5, consists of:

- An electromagnetic shaker [42].
- A control unit [43].
- Accelerometer [44].
- Oscilloscope [45] and multimeter [46].

Table 2.4: VEH test parameters

Parameter	**Value**
Frequency range	50 – 65 Hz
Slew rate	1 Hz/min
Acceleration amplitude	0.5 g
Test period	15 min/test

Shaker, control unit and accelerometer acting as a close loop circuit. The control unit defines test frequency, acceleration amplitude and slew rate, while the accelerometer attached to the shaker platform measures acceleration and sends a feedback signal to the control unit. The accelerometer sensitivity is 500 mV/g. The test setup parameters are listed in Table 2.4. This experimental setup was deployed to compare the performance of the 30 and 80 turns VEHs.

2.5 Frequency response of the 80 Turns VEH

2.5.1 Open Circuit Tests

The frequency response of the open circuit voltage for the 80 turns VEH is shown in Figure 2.6. The peak-to-peak voltage is obtained for an acceleration amplitude of $A_o = 0.5\,\mathrm{g}$ and the frequency is swept in the range of 50–65 Hz. Maximum $V_{p-p} = 3.65\,\mathrm{V}$ was acquired at the resonant frequency $f_\circ = 57.2\,\mathrm{Hz}$. The frequency-response curve is tilted to the left indicating a softening (net) nonlinearity. The effect of the nonlinear forces on the oscillation are small, this could be could be a reason of the small acceleration amplitude applied. Where the nonlinear VEH acts as a linear since the nonlinear component is smaller than the linear component < 1 [47].

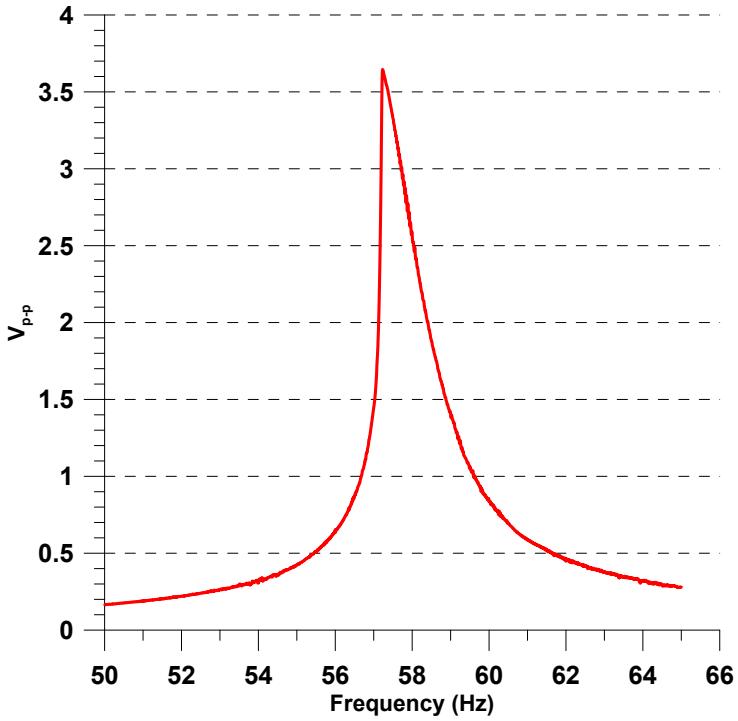

Figure 2.6: Open circuit frequency response

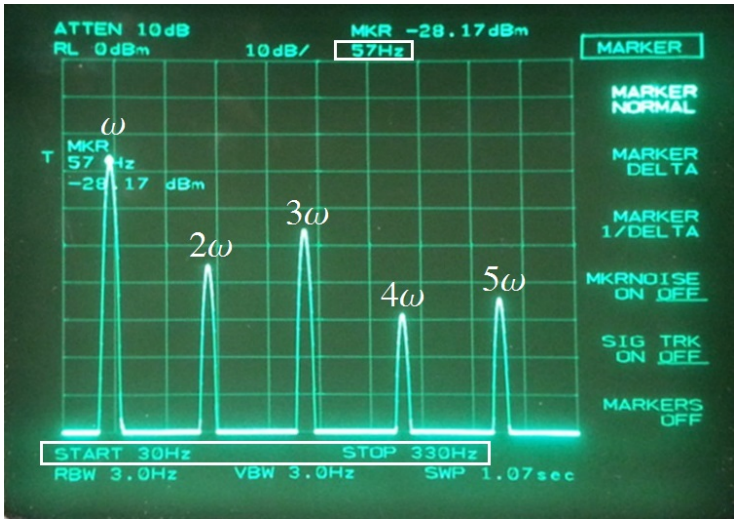

Figure 2.7: FFT signal analysis

A spectrum analyzer was used to study the frequency spectrum of the VEH output voltage for an excitation near resonance at ω=57 Hz. The spectrum bandwidth was set to 30–330 Hz to capture higher harmonics present in the output signal. The FFT of the signal is shown in Figure 2.7. The peaks observed at $2\,\omega$ and $4\,\omega$ indicate the presence of a quadratic nonlinearity in the harvester dynamics. On the

other hand, the peaks at $3\,\omega$ and $5\,\omega$ indicate the presence of a cubic nonlinearity. The presence of higher power (higher peaks) in the odd harmonics than exists in the even harmonics indicates that the cubic nonlinearity is dominant and softening.

2.5.2 Closed Circuit Tests

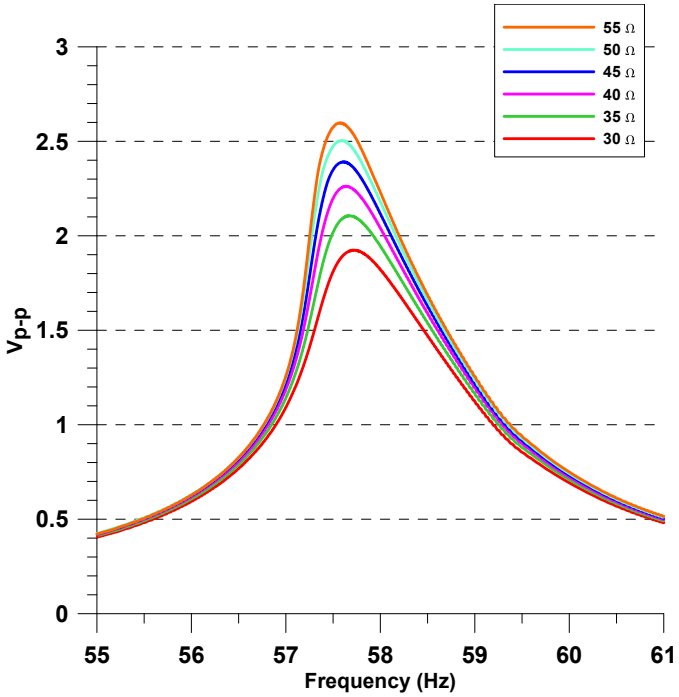

Figure 2.8: Frequency-response curves of the 80 turns VEH for R_L=30–55 Ω

Two experiments were conducting to determine the optimal load, maximum power, and linearity of the VEH.

- **Experiment # 1:** The harvester circuit was closed by connecting the leads of the coil to a potentiometer allowing us to vary the VEH resistive load R_L from 30 Ω to 55 Ω in increments of 5 Ω. The acceleration amplitude was set to 0.5 g and the frequency was swept from 55 to 61 Hz while the controller was used to capture the peak-to-peak magnitude of the output voltage V_{p-p}. The resulting frequency-response curves are shown in Figure 2.8.

  The curves show the resistive load has minimal effect on the harvesting bandwidth the VEH, which remains throughout at about 2 Hz, from 57 Hz to 59 Hz.

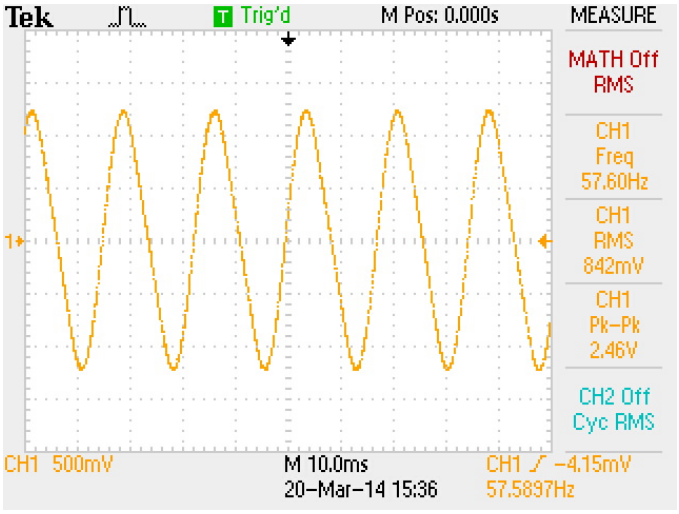

Figure 2.9: Output voltage waveform captured using an oscilloscope at resonance and optimal load

In this range, the VEH can produce $> 1\,V_{p-p}$. The softening nonlinearity results in a downward shift in the resonance frequency as the output voltage increases. This increase in voltage is due to increased load resistance R_L resulting in a decrease in electrical damping c_e.

- **Experiment # 2:** An oscilloscope and a multimeter were used to capture and measure the voltage V_{RMS} across the resistive load R_L as it was increased from 5 to 100 Ω in increments of 5 Ω . The acceleration amplitude was held at 0.5 g and measurements were taken at resonance in each stage.

2.5.3 Output Voltage and Power

Two approaches were used to determine V_{RMS}. The RMS voltage was calculated from oscilloscope captured time-domain waveform, Figure 2.9, using the average root mean square equation

$$V_{RMS} = \sqrt{\frac{\sum_i V_i^2}{N}} \tag{2.16}$$

where N is the number of samples and V_i is the discretized voltage. It was also measured directly across the resistive load via a voltmeter. The results of both approaches were identical. Since the coil inductance is negligible (L=125 mu H),

Table 2.5: Voltage and power at various resistive loads

Load Ω	**Voltage** (mV)	**Power** (mW)
5	149.23	4.45
10	286.90	8.23
15	399.00	10.61
20	510.20	13.02
25	575.70	13.26
30	641.40	13.71
35	699.40	13.98
40	**756.20**	**14.30**
45	791.10	13.91
50	824.10	13.58
55	849.20	13.11
60	871.20	12.65
65	900.00	12.46
70	920.00	12.09
75	935.21	11.66
80	958.10	11.47
85	966.80	11.00
90	981.90	10.71
95	992.40	10.37
100	1007.10	10.14

we assume the load is a purely resistive and calculate the output power P_{out} using the equation

$$P_{out} = \frac{V_{RMS}^2}{R_L} \tag{2.17}$$

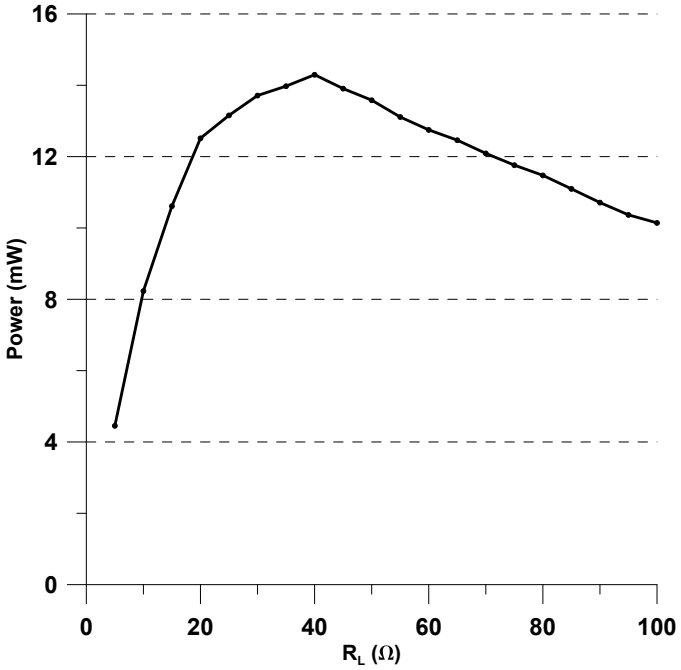

Figure 2.10: Output power as a function of resistive load

The transduction output power P_{out} and voltage V_{RMS} listed in Table 2.5 were determined at resonance (peak voltage) and base acceleration amplitude of 0.5 g as a function of the resistive load R_L. The output power P_{out} is shown in Figure 2.10 showing a maximum output power of 14.3 mW at the corresponding 'optimal' load of $R_L = 40\,\Omega$.

2.6 Comparison of the 30 and 80 Turns VEHs

The frequency-response curves of the 30 and 80 turns VEHs obtained at their total optimal loads $R_L + R_C$ of $13\,\Omega$ and $44\,\Omega$, respectively, are shown in Figure 2.11. Results show an increase of V_{p-p} from 0.7 to 2.3 between the 30 and 80 turns VEHs. This voltage increase is due to improved coil location with respect to magnetic field and the use of more turns as per Equation (1.5). The change in optimal load is due to improved coil chip design leading to lower mechanical losses in the harvester and a higher Q_m of 70.06. This is another reason for the 80 turns VEH increased output power.

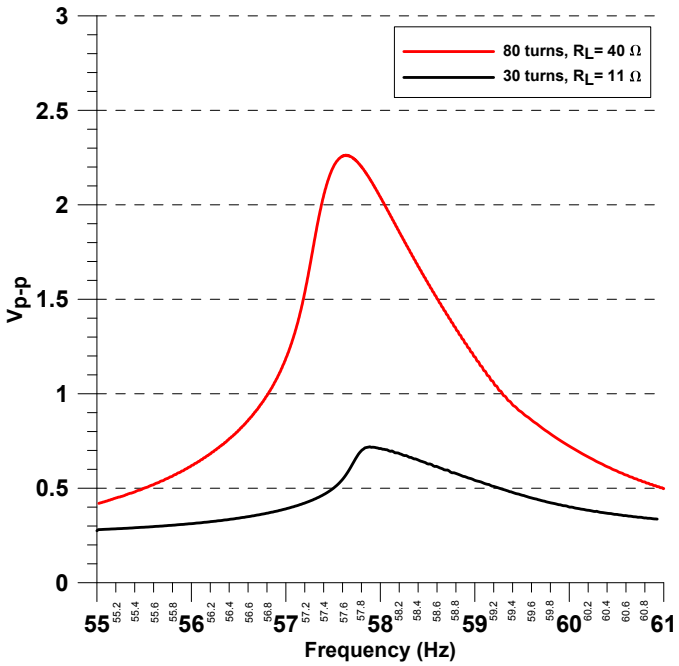

Figure 2.11: Frequency-response of the 30 and 80 turns VEHs

2.7 Summary

In this chapter, a cantilever VEH introduced and its specifications listed. The VEH is re-designed to optimize its output power using 3D printer where a coil-chip was designed to carry 80 turns instead of 30 turns.

The Evaluation experiments conducted to analyze the 80 turns VEH frequency response at open and close circuit. In addition to, different parameter identification utilized such as backbone technique, quality factor estimation and transduction parameter estimation.

A comparison made between the 80 and 30 turns frequency response including the positive and negative effects of increasing coil number of turns on linearity, output power and optimal load. Results show the maximum output power extracted using the 30 turns VEH is $\sim 6.1\,\mathrm{mW}$ at $0.5\,\mathrm{g}$, the resonant frequency f_n $58\,\mathrm{Hz}$ and the optimal load is $11\,\Omega$. On the other hand, the 80 turns VEH increases the maximum output power to $\sim$ $14.3\,\mathrm{mW}$ at $0.5\,\mathrm{g}$, its resonant frequency is f_n = $57.7\,\mathrm{Hz}$ and its optimal load is $40\,\Omega$.

Chapter 3

Power Unit Modeling and Realization

3.1 Power Unit

The power unit consists of three parts: VEH, rectification circuit and smoothing capacitor. The power unit scavenges kinetic energy and delivers DC power.

3.1.1 Rectification Circuit

We adopted the passive AC/DC conversion circuit architecture proposed by Peters *et al* [48]. This architecture overcomes the drawbacks of diodes and active control circuits; namely lower efficiency and higher power consumption. The circuit consists of four MOSFETs, two P-channel [49] and two N-channel [50], configured as a full-wave bridge rectifier as shown in Figure 3.1. It is fabricated on $2.54 \times 2.54\,\text{cm}$ PCB and shown in Figure 3.2.

During the input voltage V_{in} positive half-cycle, P-M1 and N-M2 conduct current; while, P-M2 and N-M1 are in cutoff mode. During the negative half-cycle, P-M2 and N-M1 conduct current while P-M1 and N-M2 are in cutoff mode. The MOSFETs threshold voltage V_{th} and gate voltage V_g control the current path; a P-channel MOSFET requires negative gate voltage and a N-channel MOSFET re-

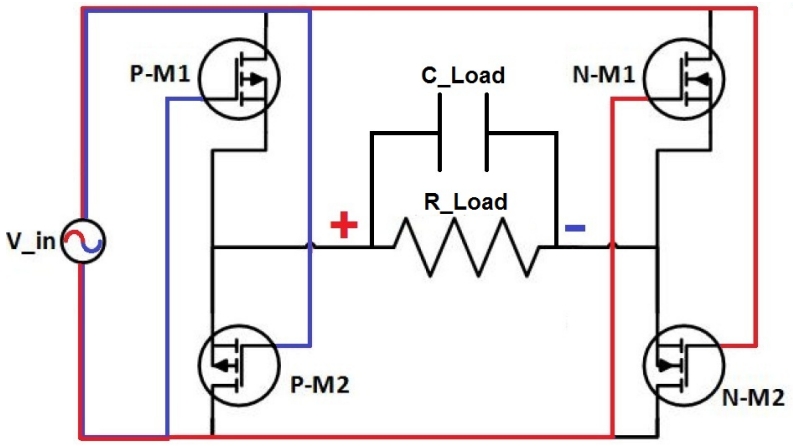

Figure 3.1: Schematic diagram of the full-wave bridge rectification circuit

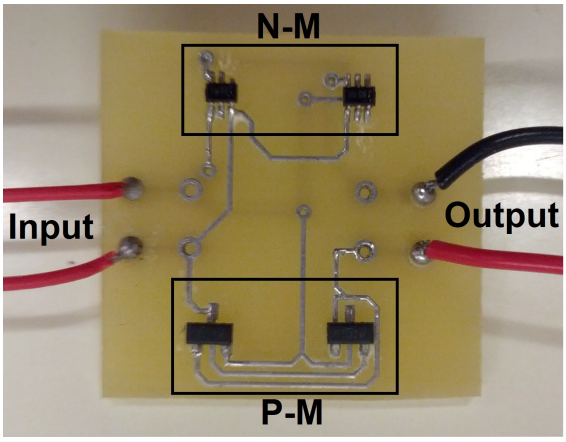

Figure 3.2: Picture of the fabricated full-wave rectification circuit

quires positive gate voltage to conduct. The MOSFETs in each half-cycle drive the current to reach the load in the same direction. As a result, the negative half-cycles (black curve) flip to positive cycles (blue curve) and the frequency of the output voltage is doubled, Figure 3.3.

The P-channel MOSFETs conduct at $V_{th} = -0.4\,\mathrm{V}$ and the N-channel at $V_{th} = 0.4\,\mathrm{V}$. Hence, the rectifier requires at least $\pm 0.4\,\mathrm{V}$ input voltage to control the MOSFETs gates. Because of nonidealities, losses in MOSFETs internal resistance R_{ds}, switching losses between cutoff and conduction states and current leakage, the rectifier requires more than $0.4\,\mathrm{V}$ to control the MOSFETs.

To complete the AC/DC conversion process electrolytic smoothing capacitors are introduced to reduce the ripples of the rectified signal, the green and orange

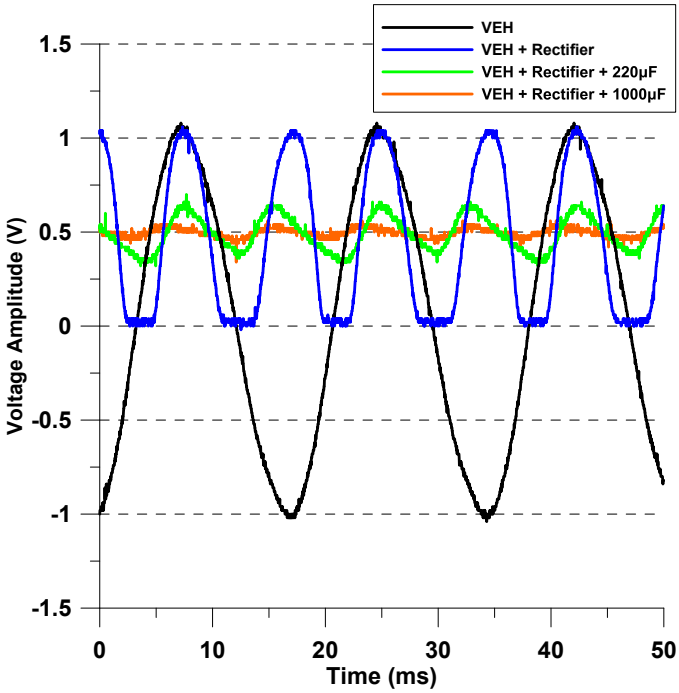

Figure 3.3: VEH output voltage waveforms measured across R_L=40 Ω

curves shown in Figure 3.3. We calculated the power conversion efficiencies at different output stages using the equation:

$$\begin{aligned} P_{out} &= \int_{t}^{t+T} V_{out} I_{out}\, dt \\ P_{in} &= \int_{t}^{t+T} V_{in} I_{in}\, dt \\ \eta_p &= \frac{P_{out}}{P_{in}}\, 100\% \end{aligned} \tag{3.1}$$

where P_{out} is the output power and P_{in} is the input power into the power management module.

3.1.2 Power Factor (PF)

The introduction of a capacitor into the rectification circuit delays the voltage signal with respect to the current signal. The phase angle between voltage and current θ (due to reactance) reduces the output power. This reduction is described by a

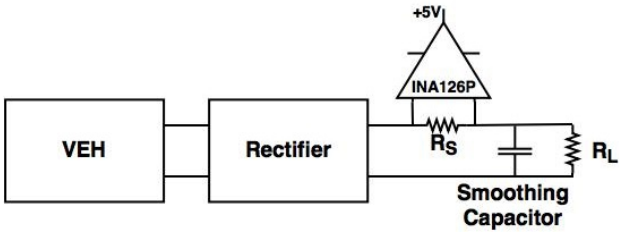

Figure 3.4: A schematic diagram of the current sensing circuit

power factor PF calculated as [51]

$$PF = \cos\,\theta \tag{3.2}$$

The voltage-current phase difference θ is calculated as

$$\theta = \frac{\Delta t}{T} \times 360 \tag{3.3}$$

where Δt is the time delay of the voltage peak with respect to the current peak and T is the signal period. We can calculate the average output power using the power factor as

$$P_{avg} = V_{out} \times I_{out} \times \cos\,\theta \tag{3.4}$$

We measured the rectifier output current using the circuit introduced in Figure 3.4. An instrument amplifier (INA126P) was used to measure the current passing through a sensing resistance R_S. This circuit amplifies the current signal, so that it can be detected using an oscilloscope since the VEH output current is low.

3.2 Power Unit Evaluation

The performance of the power unit is studied at three stages in the power conversion process as shown in Figure 3.5:

Stage 1: The output of the VEH.

Stage 2: The output of the VEH and rectification circuit.

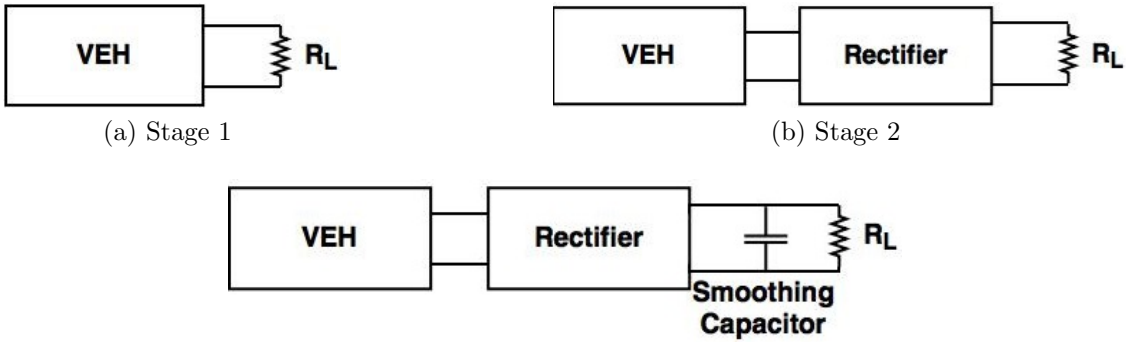

(a) Stage 1

(b) Stage 2

(c) Stage 3

Figure 3.5: Stages of the conversion process

Stage 3: The output of the VEH with rectification circuit and smoothing capacitor.

In the following, we compare the output voltage, power, and efficiency among the three stages. Moreover, we analyze power losses throughout the unit and optimal resistance.

3.2.1 Output Voltage

The output voltage waveforms of the three stages are shown in Figure 3.3. They were measured across a resistive load of $R_L = 40\,\Omega$ under base acceleration amplitude of $A = 0.5\,\text{g}$. These waveforms are:

- Stage 1 output voltage (black curve) has an AC signal waveform with peak voltage $V_p = 1.069\,\text{V}$ and $V_{RMS} = 0.756\,\text{V}$.

- Stage 2 output voltage (blue curve) is a rectified signal with peak voltage $V_p = 1.045\,\text{V}$ and $V_{RMS} = 0.739\,\text{V}$. A small phase-different between the harvester output and rectified signal is observed. It may be a result of the MOSFET's internal capacitance.

- Stage 3 involved two test cases of $220\,\mu\text{F}$ and $1000\,\mu\text{F}$ smoothing capacitors. The output voltage of the $220\,\mu\text{F}$ case (green curve) shows a peak voltage of $V_p = 0.863\,\text{V}$ and RMS voltage of $V_{RMS} = 0.610\,\text{V}$. The output voltage of the

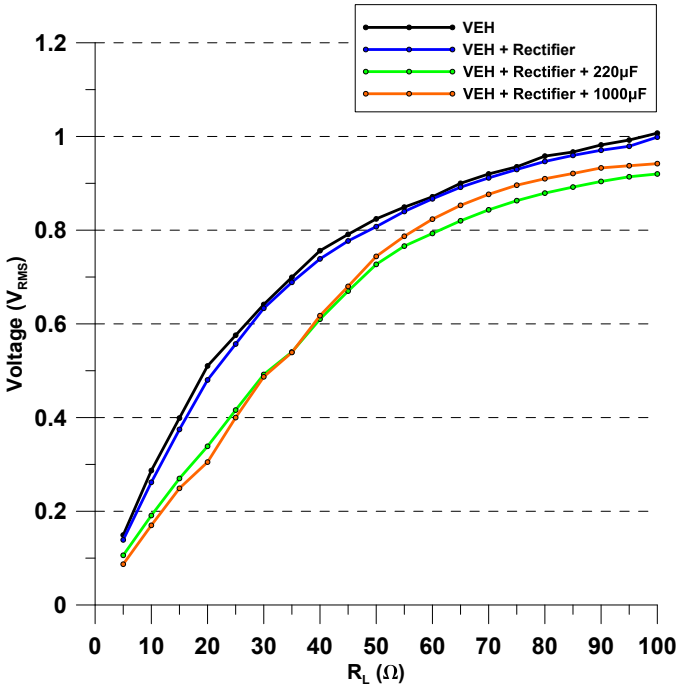

Figure 3.6: VEH output voltage as a function of R_L

1000 μF case (orange curve) shows a peak voltage of $V_p = 0.873\,\text{V}$ and RMS voltage of $V_{RMS} = 0.617\,\text{V}$.

This experiment was repeated for resistive loads in the range of 5–100 Ω. The measured RMS voltage is shown in Figure 3.6 as a function of R_L. The voltage efficiency shown in Figure 3.7, was calculated using this equation

$$\eta_V = \frac{V_{out}}{V_{in}}\,100\% \tag{3.5}$$

where V_{out} and V_{in} are the output and input voltages of the power management module. The rectified voltage efficiency at stage 2 is 97.60 % at load resistance of $R_L = 40\,\Omega$. The voltage efficiency at stage 3 is 80.67 % for 220 μF and 81.66 Ω for 1000 μF calculated at $R_L = 40\,\Omega$.

The initial increase in voltage efficiency is due to the increase in output voltage as load resistance increases. As a result, the fraction of the harvesting cycle stopped (lost) by the rectifier decreases.

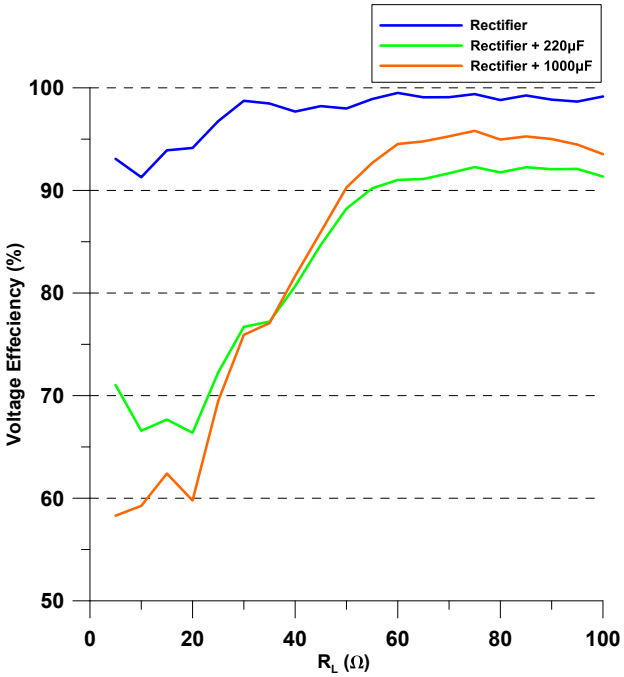

Figure 3.7: VEH output voltage efficiency as a function of R_L

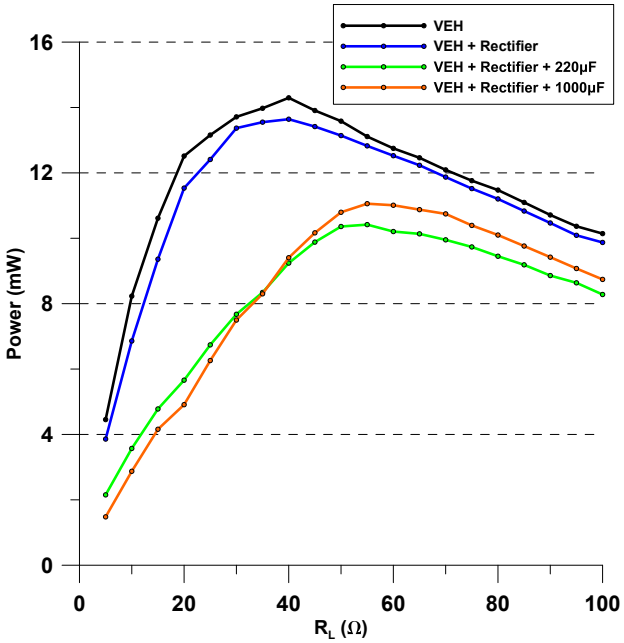

Figure 3.8: Output power as a function of R_L in the three conversion stages

3.2.2 Output power

The maximum output power and power efficiencies η_p obtained for the three conversion stages of the power unit are shown in Figures 3.8 and 3.9.

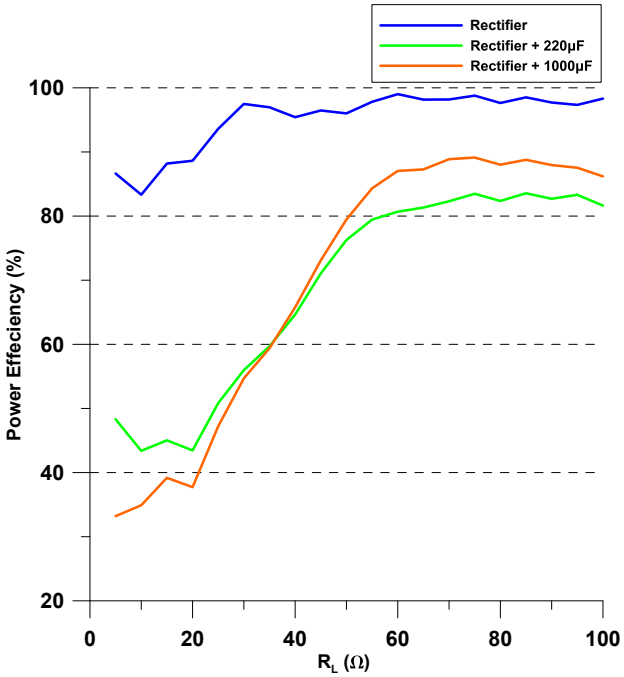

Figure 3.9: Power efficiency as a function of R_L in the three stages

The energy harvester output (stage 1) provides an optimal power of 14.30 mW at the optimal resistance $R_L = 40\Omega$. The power obtained from the VEH once the rectification circuit is introduced (stage 2) drops to 13.64 mW but the optimal load remains at $R_L = 40\Omega$. This power reduction is due to rectification losses. The power efficiency of the rectification process is 95.4 %. Introducing a smoothing capacitor adds a reactive load to the power unit that decreases the VEH power efficiency η_p to 79.45 % and 87.04 % at 220 and 1000 μF, respectively, and increases the optimal load to $R_L = 55\,\Omega$. The maximum power obtained are 10.42 and 11.06 mW at 220 and 1000 μF respectively.

The voltage waveforms in Figure 3.10 describe the output voltage for various smoothing capacitors (brown, green and orange curves). It also describes the VEH output current (black curve) and the phase difference between the voltage and current. This figure shows that increasing the capacitance from 100 to 1000 μF increases the phase angle θ from 33.08^o– 43.84^o and decreases the ripple. The highest PF is determined to be 0.837 at 100 μF and the lowest PF to be 0.721 at 1000 μF as listed in Table 3.1. The phase angle θ and power factor PF in the three cases

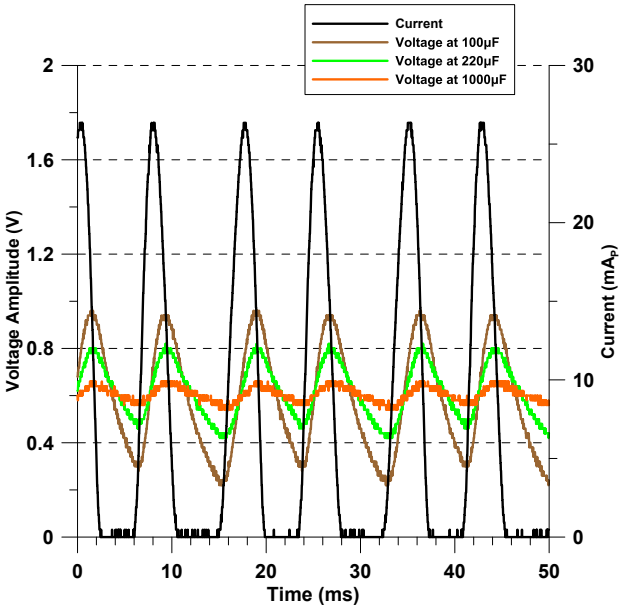

Figure 3.10: The relationship between V_{out} and I_{out} at stage 3 for R_L=55Ω

were calculated using Equations (3.3) and (3.2), respectively.

Table 3.1: voltage-current Phase Angles

Capacitance μF	Phase angle θ	PF
100	33.08^o	0.837909
220	37.00^o	0.798636
1000	43.84^o	0.721277

From these experiments we conclude that increasing the capacitance of the smoothing capacitor increases the voltage-current phase angle, the output voltage and the optimal load while minimizing the ripples. A summary of the voltage, power, and power efficiency of the harvesting stages appears in Table 3.2:

Table 3.2: Obtained voltage, power, η_p and optimal load of the power unit

LoadΩ	**Case 1**		**Case 2**			**Case 3**					
							220 μF			1000 μF	
	mV	mW	mV	mW	η_P %	mV	mW	η_P %	mV	mW	η_P %
5	149.2	4.45	138.9	3.86	86.63	106.0	2.15	48.31	87.0	1.48	33.21
10	286.9	8.23	261.9	6.86	83.33	191.0	3.57	43.39	170.0	2.87	34.90
15	399.0	10.61	374.7	9.36	88.19	270.0	4.78	45.03	249.0	4.16	39.18
20	510.2	13.02	480.3	11.53	88.62	338.7	5.66	43.46	305.0	4.91	37.73
25	575.7	13.26	557.0	12.41	93.61	416.0	6.74	50.83	400.0	6.26	47.22
30	641.4	13.71	633.3	13.37	97.49	492.0	7.68	55.97	487.0	7.50	54.69
35	699.4	13.98	688.7	13.55	96.96	540.0	8.34	59.70	539.0	8.30	59.39
40	**756.2**	**14.30**	**738.7**	**13.64**	**95.43**	610.0	9.24	64.64	617.5	9.40	65.78
45	791.1	13.91	777.0	13.42	96.47	670.0	9.88	71.06	680.0	10.17	73.10
50	824.1	13.58	807.5	13.04	96.01	727.0	10.36	76.27	744.0	10.80	79.48
55	849.2	13.11	839.9	12.83	97.82	**766.0**	**10.42**	**79.45**	**787.0**	**11.06**	**84.33**
60	871.2	12.65	866.9	12.53	99.02	793.0	10.21	80.68	823.5	11.01	87.04
65	900.0	12.46	891.7	12.23	98.16	820.0	10.14	81.33	853.0	10.88	88.87
70	920.0	12.09	911.6	11.87	98.18	843.4	9.95	82.31	876.5	10.75	89.13
75	935.2	11.66	929.5	11.52	98.78	863.0	9.73	83.48	896.0	10.39	88.01
80	958.1	11.47	946.7	11.20	97.63	879.1	9.45	82.36	909.8	10.10	88.78
85	966.8	11.00	959.6	10.83	98.52	892.0	9.19	83.55	921.0	9.76	87.96
90	981.9	10.71	970.6	10.47	97.71	904.0	8.86	82.70	932.9	9.42	87.54
95	992.4	10.37	979.1	10.09	97.34	914.0	8.64	83.32	936.5	9.08	87.54
100	1007.1	10.14	998.6	9.97	98.32	920.0	8.28	81.64	942.0	8.74	86.19

3.3 Power Unit Modeling

Mathematical modeling is an efficient way to analyze and optimize systems. We couple the VEH and the power management subsystems into an electromechanical

model in order to better understand their interactions and to optimize the power unit as a whole.

Elvin *et al* [52] proposed a coupled electromechanical model for an electromagnetic vibration based power unit. They estimated the electromechanical system parameters including the magnetic flux density found using Biot-Savarat Law. Wang *et al* [53] presented another method to estimate the magnetic flux as a piecewise function of the coil position with respect to the magnets.

3.4 Parameter Identification

Parameter identification is a part of the modeling process in which we estimate the model parameters from experimentally measured data. The acquired parameters are used to solve the model equations.

3.4.1 Natural Frequency

We used a nonlinear system identification technique, the backbone technique [55], to determine the natural frequency ω_n of the VEH. We created a parabolic fit for the resonance frequency $f_\circ$ as a function of the peak voltage $a_\circ$ from the frequency-response curves obtained in experiment # 1, Figure 2.8. The built-in Mathematica function **Fit** was used to obtain the quadratic fit,

$$f_\circ(a_\circ) = 57.85 - 0.0406\, a_\circ^2 \tag{3.6}$$

The natural frequency constitutes the intercept of the parabola with the horizontal axis in Figure 3.11, $f_n = 57.85\,\text{Hz}$.

3.4.2 Quality Factor

The quality factor Q of an energy harvester describes the harvesting bandwidth. The half-power bandwidth method is traditionally used to calculate the quality

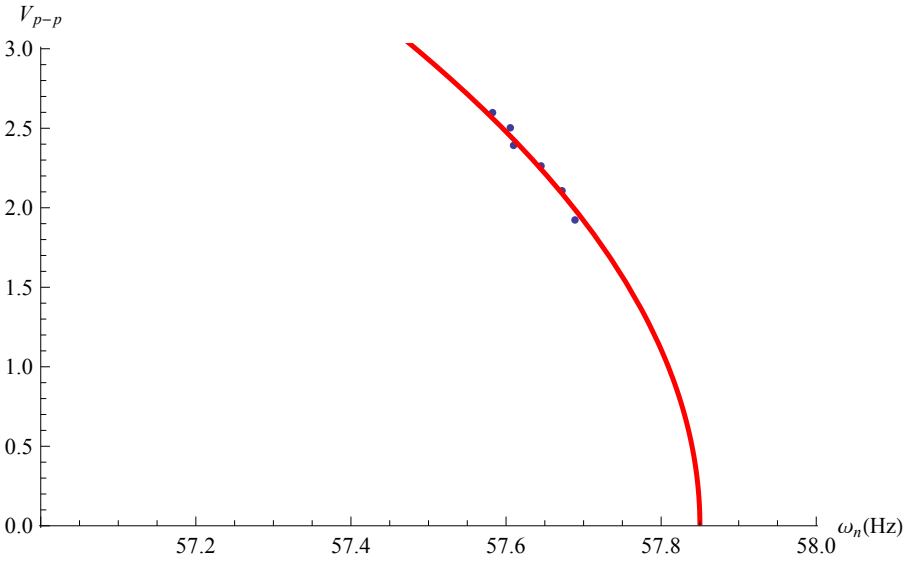

Figure 3.11: The backbone curve

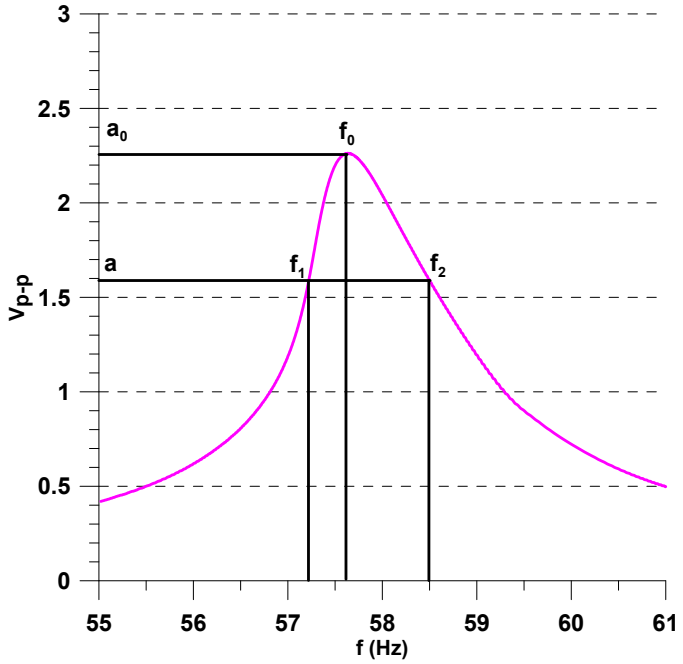

Figure 3.12: Estimation of the quality factor

factor for linear systems [56]

$$Q = \frac{f_n}{\Delta f} \tag{3.7}$$

where the bandwidth Δf is the difference between the frequencies f_2 and f_1 where the response amplitude $a = \frac{a_n}{\sqrt{2}}$. Davis [57] introduced a more accurate formula to

estimate the quality factor for nonlinear systems

$$Q = \frac{f_n}{\Delta f}\sqrt{\frac{a_\circ^2}{a^2} - 1} \tag{3.8}$$

where $a_\circ$ is the response amplitude at resonance, Figure 3.12.

The mechanical quality factor was estimated from the open-circuit frequency-response curve shown in Figure 2.6 using Equation (3.8) as $Q_m = 70.06$. The total quality factor Q_t and the damping ratio for each of the closed-circuit frequency-response curves shown in Figure 2.8 were also calculated using Equation (3.8). They are listed in Table 3.3.

The results show that the electrical and total damping drop as the load resistance increase in agreement with the predictions of Equation (2.13). The quality factor of the system is significantly $Q > \frac{1}{2}$, which indicates that the stored energy in the system is much higher than the losses per cycle and the overall system response is lightly damped.

Table 3.3: Total quality factor at various resistive loads

R_L (Ω)	Q_t	ζ_t
30	40.314	0.01240
35	43.301	0.01240
40	46.022	0.01086
45	47.889	0.01044
50	49.571	0.01009
55	51.331	0.00974

3.4.3 Effective Mognetic Flux Density

We developed a method to estimate the magnetic flux density B using the measured mechanical quality factor Q_m and total quality factor Q_t. First, the electrical quality factor Q_e was obtained. The relationship between the mechanical, electrical and total quality factors is

$$\frac{1}{Q_t} = \frac{1}{Q_m} + \frac{1}{Q_e} \tag{3.9}$$

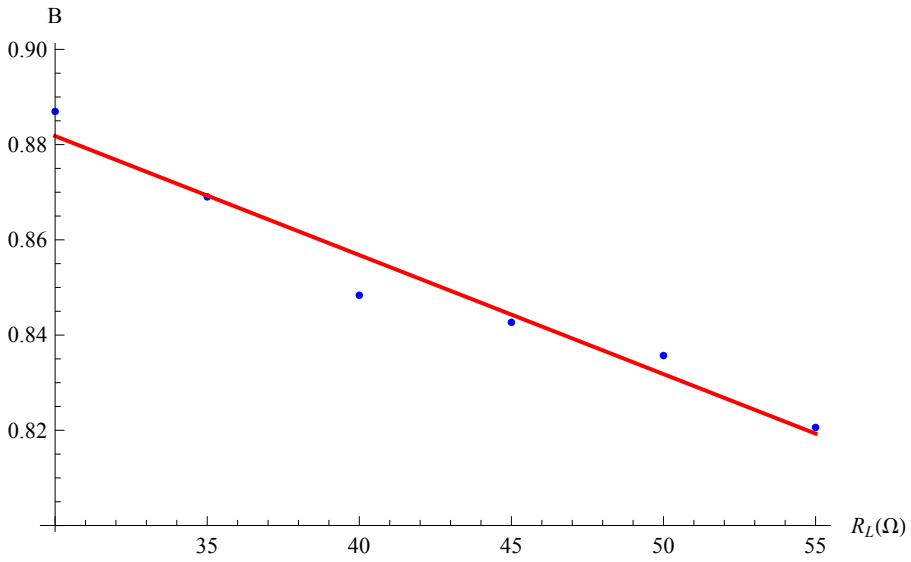

Figure 3.13: Effective magnetic flux density B as a function of R_L

which was used to evaluate Q_e as listed in Table 3.4.

The electrical quality factor is also related to the electrical damping ratio ζ_e, Equation (2.13), by

$$\begin{aligned} Q_e &= \frac{1}{2\,\zeta_e} \\ &= \frac{m\omega_n(R_L + R_c)}{(B\ell)^2} \end{aligned} \tag{3.10}$$

Substituting for Q_e, from Equation (3.9) into Equation (3.10), and solving the resulting equation for $B\ell$, we obtain

$$B\ell = \sqrt{m\omega_n(R_L + R_c)}\sqrt{\frac{Q_m - Q_t}{Q_m Q_t}} \tag{3.11}$$

This equation was used to calculate the transduction coefficient $B\ell$ (Table 3.4) for each of the closed-circuit frequency-response curves of Figure 2.8.

The effective length of the coil can be estimated from the coil-chip geometry, Figure A1, and the number of coil turns N using the relationship,

$$\ell = 2N \times (\frac{d_1 + d_2 + d_c}{2}) \tag{3.12}$$

where d_1 is the coil outer length, d_2 is the coil core length, and d_c is the wire thickness. We found the effective length to be $\ell = 2.33\,\mathrm{m}$. The calculated average magnetic flux density B, from the transduction coefficient $B\ell$ and the coil effective length ℓ, are listed in Table 2.2.

Table 3.4: Variation of transduction coefficient $B\ell$ and electrical quality factor Q_e with R_L

$R_L\,(\Omega)$	B (T)	$B\ell$	Q_e
30	0.8869	2.069	94.950
35	0.8690	2.027	113.370
40	0.8483	1.979	134.134
45	0.8426	1.966	151.328
50	0.8356	1.949	169.503
55	0.8205	1.914	192.015

The effective flux density is shown in Figure 3.13 as a function of load resistance. We note that it decreases linearity with R_L following the relationship:

$$B(R_L) = 0.957 - 0.0025R_L \tag{3.13}$$

The drop in magnetic flux is proportional to the coil stroke. At equilibrium, the coil is placed at the centers of the magnets (maximum B). As it oscillates away from equilibrium, it experiences lower flux density, Figure 2.4. The value of B identified above represents a weighted average of B. As resistance increases, total damping drops allowing the coil oscillations $x(t)$ to increase and reach regions where B drops further.

3.4.4 Optimal Resistance

The optimal resistance for a linear VEH is obtained by taking the derivative of the average electrical output power P_e, Equation (2.12), with respect to the electrical

damping ratio ζ_e and setting it equal to zero.

$$\begin{aligned}\frac{dP_e}{d\zeta_e} &= -\frac{mA_o^2\zeta_e\omega_n}{2(\zeta_e+\zeta_m)^3} + \frac{mA_o^2\omega_n}{4(\zeta_e+\zeta_m)^2} \\ &= -\frac{mA_o^2\omega_n(\zeta_e-\zeta_m)}{4(\zeta_e+\zeta_m)^3} \\ &= 0 \end{aligned} \tag{3.14}$$

which results in the well known impedance matching condition: $\zeta_e = \zeta_m$. In other words, to maximize output power, the impedance matching theory mandates that the mechanical and electrical quality factor should be equal and twice the total quality factor [58].

Our results show a mismatch between the mechanical and electrical quality factors, $Q_e = 134.134$ and $Q_m = 70.060$, at the maximum output power of the VEH (R_L=40 Ω). This impedance mismatch is a result of the nonlinearity in our VEH. Equation (2.12) assumes a linear electromechanical model to estimate the output power. On the other hand, given the nonlinear behavior of our VEH optimal power is obtained when $\zeta_e \simeq \frac{1}{2}\zeta_m$

3.5 Electromechanical Model

We present an electromechanical model of the power unit and identify its parameters. Mechanical and electrical coupling forces are included in the model to derive the coupling relationship. This model was solved using two methods: numerically using Mathematica's built-in function **NDSolve** and analytically using operator notation [54]. Moreover, the eigenvalues were calculated to determine damping, stability and the effect of the coupling on the system response. Finally, we compared the obtained model frequency-response curves, voltage and power output to the experiment results to validate it.

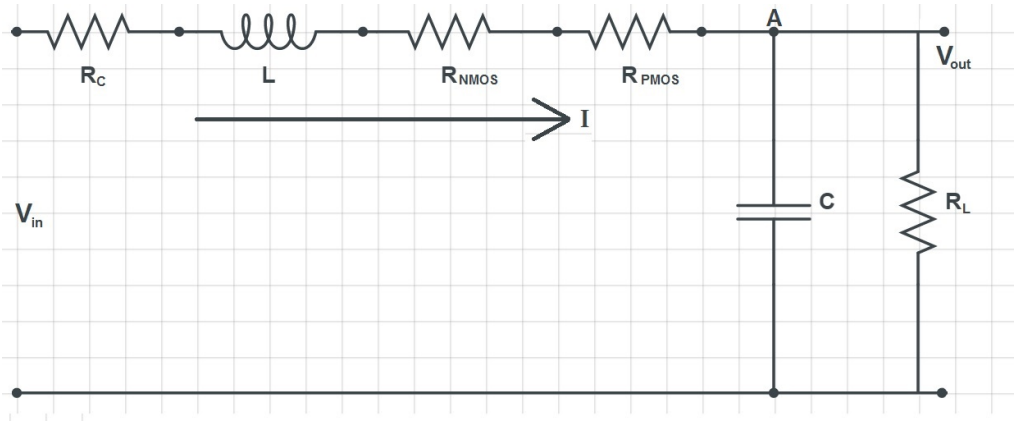

Figure 3.14: The equivalent circuit model of the power management module

3.5.1 Power Management Circuit Model

The equivalent circuit model of the power management module is shown in Figure 3.14. The model presents all the components of the module including coil parasitic resistance R_C, coil inductance L, MOSFETs internal resistance (R_{NMOS} and R_{PMOS}), smoothing capacitor C and resistive load R_L. The MOSFETs capacitance was ignored assuming it is negligible [59].

Applying Kirchhoff's Voltage Law (KVL) to the electrical equivalent circuit, we obtain:

$$-V_{in} + R_p\ I + L\dot{I} + V_{out} = 0 \tag{3.15}$$

where (R_pI) is the voltage across parasitics resistance (R_p=$R_C + R_{NMOS} + R_{PMOS}$) and ($L\dot{I}$) is the voltage across the inductance L. The smoothing capacitor C and load resistance R_L share the same output voltage V_{out}. We applied Kirchhoff's Current Law (KCL) on node A to obtain:

$$\begin{aligned} I &= I_C + I_R \\ &= C\dot{V}_{out} + \frac{V_{out}}{R_L} \end{aligned} \tag{3.16}$$

Taking the time derivative of Equation (3.16) we get:

$$\dot{I} = C\ddot{V}_{out} + \frac{\dot{V}_{out}}{R_L} \tag{3.17}$$

Using Equation (3.16) and (3.17) to substitute for I and $\dot{I}$ in Equation (3.15), we obtained a second-order model of the electrical subsystem as a function of V_{out}.

$$\begin{aligned} V_{in} &= R_p(C\dot{V}_{out} + \frac{V_{out}}{R_L}) + L(C\ddot{V}_{out} + \frac{\dot{V}_{out}}{R_L}) + V_{out} \\ &= R_pC\dot{V}_{out} + \frac{R_p}{R_L}V_{out} + LC\ddot{V}_{out} + \frac{L}{R_L}\dot{V}_{out} + V_{out} \\ \ddot{V}_{out} &= \frac{1}{LC}(V_{in} - R_pC\dot{V}_{out} - \frac{L}{R_L}\dot{V}_{out} - \frac{R_p}{R_L}V_{out} - V_{out}) \end{aligned} \tag{3.18}$$

3.6 Coupled System Model

The coupling coefficients represent the interaction forces between the mechanical and electrical subsystems. The electrical coupling force F_e arises due to the induction of current I passing in the coil as per Lorentz Law [52],

$$F_e = B\ell I \tag{3.19}$$

This force acts on the coil to oppose its motions through the magnetic field, therefore modifying the inertial mass equation of motion, Equation (2.2), to

$$\begin{aligned} \ddot{x} &= -\frac{\omega_n}{Q}\dot{x} - \omega_n^2 x - \ddot{y} - \frac{F_e}{m} \\ &= -\frac{\omega_n}{Q}\dot{x} - \omega_n^2 x - \ddot{y} - \frac{B\ell I}{m} \end{aligned} \tag{3.20}$$

Substituting the equivalent circuit current I from Equation (3.16) into Equa-

tion (3.20), we obtain the mechanical subsystem model,

$$\begin{aligned}\ddot{x} &= -\frac{\omega_n}{Q}\dot{x} - \omega_n^2 x - \ddot{y} - \frac{B\ell}{m}(C\dot{V}_{out} + \frac{V_{out}}{R_L}) \\ &= -\frac{\omega_n}{Q}\dot{x} - \omega_n^2 x - \ddot{y} - \frac{B\ell C}{m}\dot{V}_{out} - \frac{B\ell}{mR_L}V_{out} \\ &= -\mu_m\dot{x} - \omega_n^2 x - \ddot{y} - K_{bs}\dot{V}_{out} - K_b V_{out} \end{aligned} \tag{3.21}$$

We denoted:

$$K_{bs} = \frac{B\ell C}{m} \text{ (Backward stiffness)} \tag{3.22}$$

$$K_b = \frac{B\ell}{mR_L} \text{ (Backward electromechanical coupling)} \tag{3.23}$$

$$\mu_m = \frac{\omega_n}{Q} \text{ (Mechanical damping)} \tag{3.24}$$

The forward coupling between the electrical subsystem and the mechanical subsystem occurs via Faraday's Law [52]. Since the coil velocity $\dot{x}$ is perpendicular to the magnetic flux density B, we can represent the voltage induced in the coil effective length ℓ as

$$V_{in} = B\ell\dot{x} \tag{3.25}$$

Substituting the induced EMF, Equation (3.25), into the electrical subsystem model, Equation (3.18), yields

$$\begin{aligned}\ddot{V}_{out} &= \frac{1}{LC}(B\ell\dot{x} - R_p C\dot{V}_{out} - \frac{L}{R_L}\dot{V}_{out} - \frac{R_p}{R_L}V_{out} - V_{out}) \\ &= \frac{B\ell}{LC}\dot{x} - (\frac{R_p}{L} + \frac{1}{R_L C})\dot{V}_{out} - \frac{1}{LC}(\frac{R_p}{R_L} + 1)V_{out} \\ &= K_f\dot{x} - \mu_e\dot{V}_{out} - \omega_e^2 V_{out} \end{aligned} \tag{3.26}$$

where:

$$K_f = \frac{B\ell}{LC} \text{ (Electromechanical forward coupling)} \tag{3.27}$$

$$\mu_e = \frac{R_p}{L} + \frac{1}{R_L C} \text{ (Electrical damping)} \tag{3.28}$$

$$\omega_e^2 = \frac{1}{LC}(\frac{R_p}{R_L} + 1) \text{ (Electrical frequency)} \tag{3.29}$$

3.6.1 Solving the Linear System

The coupled electromechanical model, Equation (3.21) and (3.26) were solved to analyze the power unit system response. As a first cut analysis, we neglected the nonlinearity present in the magnetic field B and potentially arising from friction between the coil and magnets. We note that the effective nonlinearity is small as seen in the experimental results.

The numerical solutions of **NDSolve** and operator notation method were compared to investigate the quality of our results. The derivation of the numerical operator notation is described in the flow chart shown in Figure A3.

3.6.2 Eigenvalues

We solved the homogeneous problem of the coupled electromechanical system to determine the eigenvalues. The state-space matrix of the system is constituted from Equations (3.21) and (3.26) as

$$\begin{bmatrix} \dot{V_1} \\ \dot{V_2} \\ \dot{x_1} \\ \dot{x_2} \end{bmatrix} = \begin{bmatrix} 0 & 1 & 0 & 0 \\ -\omega_e^2 & -\mu_e & 0 & K_f \\ 0 & 0 & 0 & 1 \\ -K_b & -K_{bs} & -\omega_n^2 & -\mu_m \end{bmatrix} \begin{bmatrix} V_1 \\ V_2 \\ x_1 \\ x_2 \end{bmatrix}$$

or

$$\begin{aligned}
\dot{V_1} &= V_2 \\
\dot{V_2} &= K_f\, x_2 - \mu_e V_2 - \omega_e^2\, V_1 \\
\dot{x_1} &= x_2 \\
\dot{x_2} &= -\mu_m x_2 - \omega_n^2\, x_1 - K_{bs} V_2 - K_b V_1
\end{aligned} \tag{3.30}$$

The linear system can be written as

$$\{\dot{u}\} = [A]\{u\} \tag{3.31}$$

The determinant of the matrix $[A - \lambda I]$ is the system characteristics equation:

$$\begin{aligned}
\lambda\left(K_b K_f + \omega_e^2 \mu_m + \mu_e \omega_n^2\right) + \lambda^2\left(K_{\mathrm{bs}} K_f + \mu_e \mu_m + \omega_e^2 + \omega_n^2\right) \\
+\lambda^3\left(\mu_e + \mu_m\right) + \omega_e^2 \omega_n^2 + \lambda^4 = 0
\end{aligned} \tag{3.32}$$

The roots of this equation λ_i are the system eigenvalues.

The eigenvalues were calculated using Equation (3.32) for two cases. In the first case, we used only the mechanical subsystem model to represent an open circuit VEH where the current I passing in the electrical subsystem is zero. In the second case, we used the coupled electromechanical model and varied the resistive load R_L from $30\,\Omega$ to $55\,\Omega$, without a smoothing capacitor ($\mathrm{C} \to 0$). These two cases correspond to the experiments presented in Figures 2.6 and 2.8.

We calculated the mechanical Q_m and total Q_t quality factors from the lowest two eigenvalues λ_1 and λ_2 of case#1 and case#2, respectively. The relationship

between the eigenvalue λ and the quality factor Q can be described by [60]

$$\lambda = \sigma \pm i\,\omega_d$$
$$\omega_d = \omega_n\sqrt{1-\zeta^2} \tag{3.33}$$
$$\sigma = \zeta\omega_n$$
$$Q = \frac{\omega_n}{2\sigma} \tag{3.34}$$

The eigenvalues λ, damping ratio ζ, quality factors Q and error in Q are listed in table 3.5. The results for the total Q_t and mechanical Q_m quality factors show a reasonable agreement between experimental results listed in Table 3.3 and model predictions.

Table 3.5: Predicted quality factor

$R_L\,(\Omega)$	λ	ζ	Q	Q Error(%)
30	$-4.352 \pm 363.442\,i$	0.0119	41.752	3.6
35	$-4.055 \pm 363.444\,i$	0.0111	44.810	3.5
40	$-3.813 \pm 363.446\,i$	0.0105	47.661	3.6
45	$-3.609 \pm 363.447\,i$	0.0099	50.351	5.1
50	$-3.434 \pm 363.448\,i$	0.0095	52.915	6.7
55	$-3.281 \pm 363.449\,i$	0.0090	55.378	7.9
Open circuit	$-2.5963 \pm 363.473\,i$	0.0071	69.999	0.1

The mechanical $(\omega_d)_m$ and electrical $(\omega_d)_e$ natural frequencies were also determined from the eigenvalues as function of load resistance R_L, Table 3.6. The results show an increase of the mechanical natural frequency with the increase of the load resistance. This is a result of the drop in damping as R_L increases. As per Equation (3.33), the damping natural frequency of the harvester approaches the natural frequency of the open-circuit harvester as $R_L \to \infty$. The results also show that the determined experimental natural frequency ω_n using the backbone technique is similar to the model calculations. On the other hand, the electrical natural frequency decreases while resistive load R_L increases. The electrical natural frequency is zero at the open circuit which means the transduction circuit is not conducting current.

Table 3.6: Predicted natural frequencies

$R_L\,(\Omega)$	$(\omega_d)_m\,(\text{Hz})$	$(\omega_d)_e\,(\text{Hz})$
30	57.8436	14235.7
35	57.8438	14228.5
40	57.8440	14216.4
45	57.8441	14203.0
50	57.8442	14189.9
55	57.8443	14177.4
Open circuit	57.8485	0

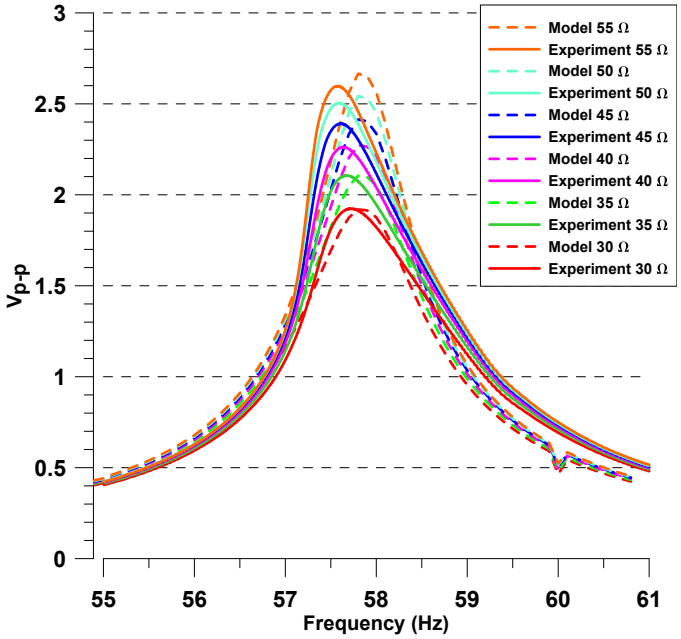

Figure 3.15: Model and experiment frequency-response curves

3.6.3 Power Unit Response

3.6.3.1 Frequency-Response Curves

We evaluated the full solution (forced response) of the coupled model in order to plot the frequency-response curves for resistive loads in the range of (30–55 Ω), Figure 3.15. The peak-to-peak voltage V_{p-p} was calculated as a function of frequency in the range of 55 to 61 Hz. The quality factor Q_t was estimated using Equation (3.8) on the frequency-response curves of Figure 3.15.

The peak-to-peak voltage V_{p-p} and total quality factor Q_t shown in Table 3.7.

The coupled model shows similar Q_t and V_{p-p} compared to the experimentally measured values. The differences in voltage are due to unaccounted for losses and the neglect of nonlinearity in the model.

Table 3.7: Frequency-response curves analysis

$R_L\,(\Omega)$	V_{p-p}	Q_t
30	1.91	41.028
35	2.09	45.542
40	2.25	46.280
45	2.40	50.305
50	2.54	52.591
55	2.67	55.095

3.6.3.2 Voltage and Power

The model output voltage and power as functions of R_L are compared to the experimental results, Figure 3.16. The model results are shown in Table 3.8. The model presents the rectified output voltage and power without the smoothing capacitor. The results show that the output voltage increases with load resistance. The model shows a maximum output power of 17.33 mW at optimal load of 30 Ω compared to 14.30 mW at 40 Ω (see Table 2.5). This shift in optimal resistance is due to the model neglect of the electromagnetic field nonlinearity. The average voltage difference between the experiment and the model is 13.3 %.

Table 3.8: Voltage and power of the coupled models as a function of R_L

$R_L\ \Omega$	**Voltage** (mV)	**Power** (mW)
5	208.56	8.70
10	360.57	13.00
15	487.83	15.87
20	579.74	16.80
25	657.51	17.29
30	721.14	17.33
35	777.70	17.28
40	827.19	17.11
45	869.61	16.80
50	904.69	16.38
55	936.77	15.96
60	961.52	15.41
65	982.73	14.86
70	1003.94	14.40
75	1025.15	14.01
80	1046.36	13.69
85	1060.50	13.23
90	1074.64	12.83
95	1088.78	12.48
100	1102.92	12.16

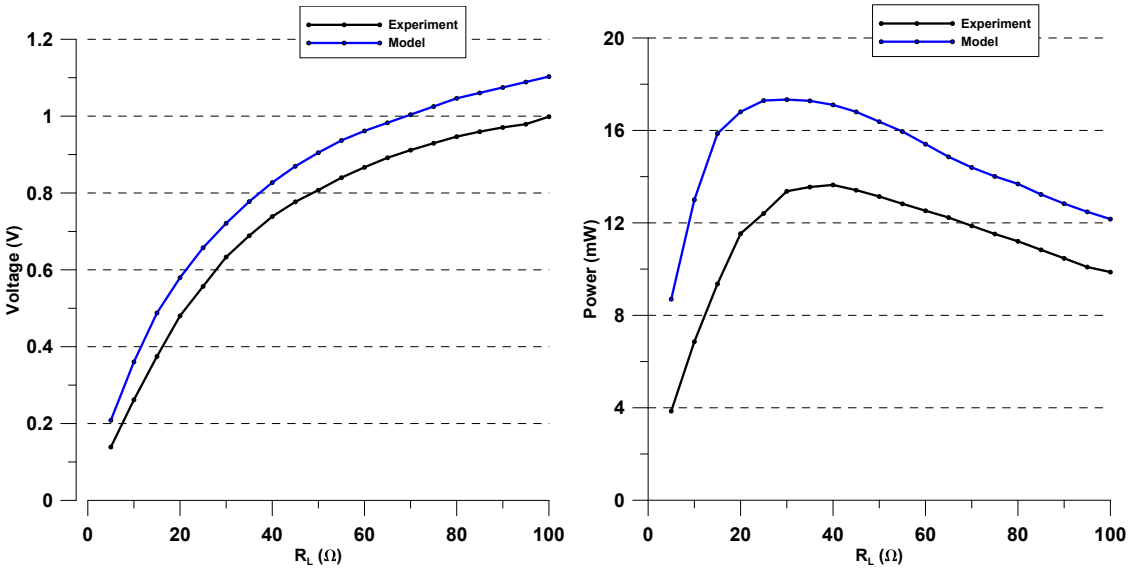

(a) Voltge (b) Power

Figure 3.16: Electromechanical model output voltage and power as functions of load resistance R_L

3.7 Summary

This chapter introduces and analyze a power management circuit consists of AC/DC full-wave bridge rectifier and smoothing capacitor. Moreover, we introduces and analyze a combined electromechanical model of a power unit comprised of an electromagnetic VEH and its power management circuit. We identified the model parameters and solve it to compare its prediction to the experimental results.

Three comparison stages listed to analyze the effect of the power management circuit on the 80 turns VEH. Introducing the rectification circuit (stage #2) decreases the output power at the 40 Ω optimal load from 14.3 mW to 13.64 mW with a power efficiency of 95.4 %. Introducing a smoothing capacitor after the rectification circuit (stage #3) decreases the output power to $\sim$ 11 mW and increases the optimal load to 55 Ω. Phase angle test conducted to analyze the change of voltage-current phase difference on different smoothing capacitors where it shows a rise in phase angle between the 220 μF and 1000 μF from 58^o to 64.84^o, respectively.

The electrical backward coupling force F_e was introduced in the linear oscillation model using Lorentz Law. On the other hand, the mechanical forward coupling force was introduced in the linearized transduction model using Faraday's Law to give us a second order differential equation as a function of voltage V(t). The electromechanical model was solved numerically using Mathematica and operator notation.

Quality factors were analytically and numerically determined using the eigenvalues from the homogeneous solution of the electromechanical model. The eigenvalues were obtained for the open circuit case and closed circuit case. In the closed circuit case we used variable resistive loads ranged between 30–55 Ω mimicking the experimental setup. The estimated quality factor Q_t at optimal load of 40 Ω is 47.661 which is similar to the experimental Q_t of 46.022. Where the quality factor error between the experiment and model is $\sim$ 3.6 %.

The frequency-response curves where determine from the particular solution of the coupled model. We used the closed circuit case to obtain the total quality factor

Q_t and voltage peak-to-peak V_{p-p} from the frequency-response curves. The coupled models show promising results compared to the experimental results. Where the determined Q_t and V_{p-p} at $40\,\Omega$ optimal load are 46.280 and 2.25 V, respectively. The estimated error between the experimental and model are $\sim 0.6\,\%$ for the Q_t and $\sim 12\,\%$ for the V_{p-p}.

We obtained output voltage and power by solving the voltage V(t) of the coupled model at various load resistances from 5–100 Ω replicating the experiment setup. The MOSFETs internal resistance was inserted in the coupled model to predict the rectifier output voltage and power. The rectifier output RMS voltage model calculated is 827.19 mV compared to 738.7 mV experimentally at $40\,\Omega$. The maximum power determined is 17.33 mW at optimal load of $R_L = 30\,\Omega$ compared to 13.64 mW at optimal load $R_L = 40\,\Omega$ experimentally.

Chapter 4

Springless Electromagnetic VEH

4.1 Introduction

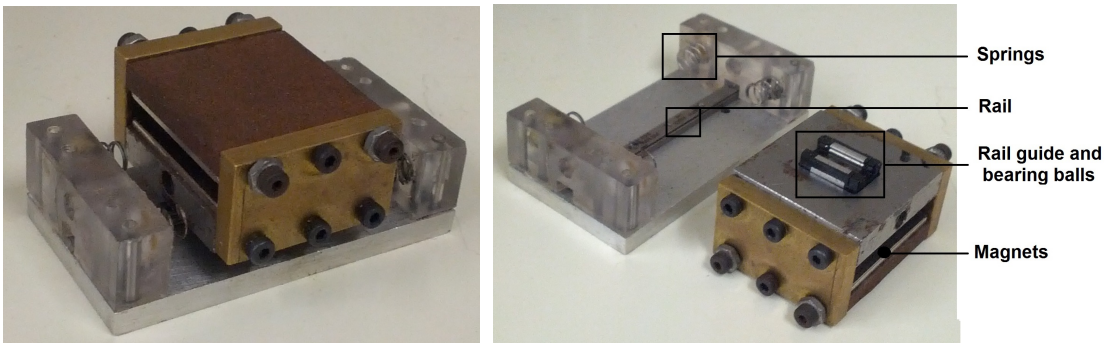

(a) Actual device (b) Device details

Figure 4.1: Springless VEH

The springless vibration energy harvester (SVEH), shown in Figure 4.1, consists of a magnetic cage of mass m, four springs, cart and rail guide. Mechanical damping, such as air resistance, spring hysteresis [61], and mechanical friction c_m occur between the rail guide and the bearing ball when the cage moves due to base excitation $y(t)$. The SVEH model can be described as

$$m\ddot{x} + c\dot{x} + F(x) = -m\ddot{y} \tag{4.1}$$

where x is the displacement of the mass and $F(x)$ is the restoration force which

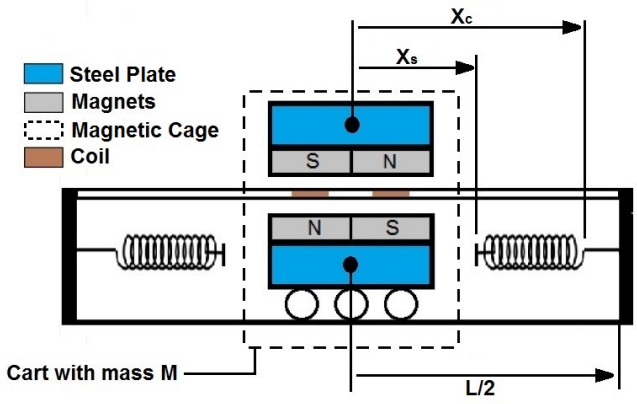

Figure 4.2: Schematic diagram of the springless VEH

varies according to the mass positions as shown in Figure 4.2. The relation between the mass displacement and limiters are as follows:

Condition#1 If $-x_s \leq x \leq x_s$ then no spring-mass contact.

Condition#2 If $x_c \leq |x| < x_s$ then spring-mass contact occur.

Condition#3 If $x_c < |x| \leq \frac{L}{2}$ then fully compressed spring contact occur.

The restoring force $F(x)$ relationship with the displacement is shown in Figure 4.3. It can be described as [62]:

$$F(x) = \begin{cases} 0 & -x_s \leq x \leq x_s \\ k_1(x - x_s) & x_s < x \leq x_c \\ k_2(x - x_c) + k_1(x_c - x_s) & x_c < x \leq \frac{L}{2} \\ k_1(x + x_s) & -x_c < x < -x_s \\ k_2(x + x_c) + k_1(x_s - x_c) & -\frac{L}{2} \leq x \leq -x_c \end{cases}$$

4.2 Springless VEH Specifications

This energy harvester consists of three main parts: base, magnetic cage and coil-chip. Where the base made of aluminum include two walls, four springs (limiters)

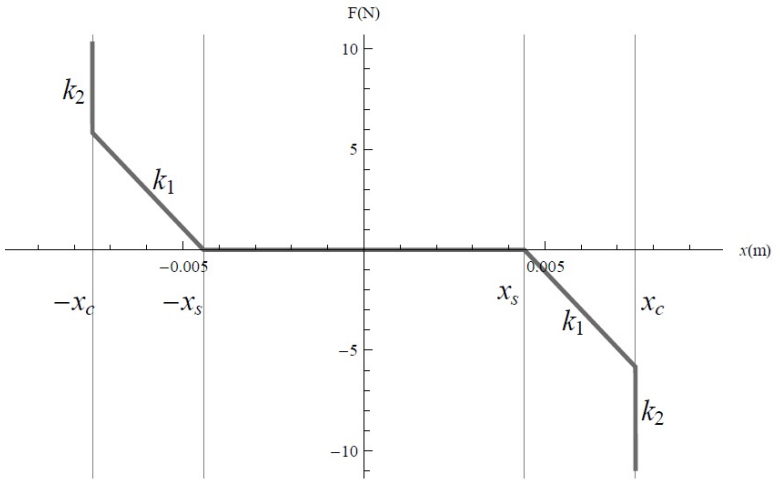

Figure 4.3: Restoring force and displacement relationship [62]

and a rail. The steel-brass cage carries four NdFeB magnets and rides over a cart, Figure 4.1. Each pair of magnets is attached to a steel plate. The brass sides are used to separate and support the steel plates leaving an air gap between each two set of magnets. A rectangular coil-chip fixed on top of the end walls as shown in Figure 4.2 to complete the transduction circuit where the magnetic flux induces electromotive force in the coil wire as the magnetic cage moves, Figure 4.2.

The SVEH has a total rail length of 41 mm including 26.2 mm magnetic cage length. The remaining 14.8 mm are divided between the springs and the rail free length. We measured the average uncompressed spring length as 4.7 mm. The average fully compressed springs length was measured as 1.65 mm. The free rail length of 5.4 mm was determined from the total rail length, cage length and springs length, where the cage moves freely without touching the springs (condition#1). These dimensions are summarized in Table 4.1.

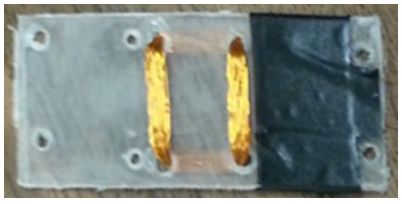

Figure 4.4: Polycarbonate coil-chip

The coil-chip shown in Figure 4.4 is made from polycarbonate and has a dimen-

Table 4.1: Springless VEH specifications

SVEH dimensions	
Total Mass	110 g
Total Length Including Walls	55.5 mm
Rail Total Length	41.0 mm
Magnets Cage Length (Along the track)	26.2 mm
Magnets Cage Width	34.3 mm
Average Length of the Springs	4.70 mm
Average Length of the Compressed Springs	1.65 mm
Rail Free Length	5.4 mm

sions of ($53.5 \times 20 \times 1.2$ mm). It can carry up to a maximum of 40 turns without magnet-coil friction. The coil specifications are listed in Table 4.2.

Table 4.2: SVEH hand-made coil specifications

25 turns coil specifications	
Type	34 AWG
Length	1750 mm
Resistance	2.4 Ω
Inductance	21 μH
40 turns coil specifications	
Type	34 AWG
Length	2800 mm
Resistance	3.6 Ω
Inductance	64 μH

4.3 Harvester Re-Design

A 3D printed coil-chip was designed to carry up to 60 turns of copper wire. The reasons of using this optimizing approach in the energy harvester had been discussed in section 2.3. The new coil-chip was made from polycarbonate-acrylonitrile butane styrene (PC-ABS) using enhanced 3D printing to act as placement for the hand-made 40 turns coil-chip. The new design has four depressions as shown in Figure 4.5 allowing for more turns.

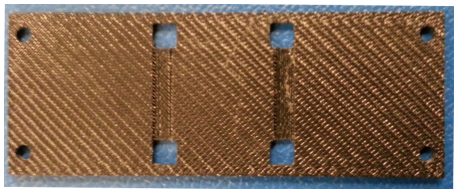

Figure 4.5: 3D printed coil-chip

The dimensions of the coil-chip ($53.5 \times 20 \times 1$ mm) are shown in the blue print in Figure A2. Each depression has dimensions of ($11.5 \times 3 \times 0.5$ mm). The coil wire has a total length of 4200 mm. The coil-chip and coil specifications are listed in Table 4.3.

Table 4.3: SVEH 3D printed coil-chip specifications

60 turns coil specifications	
Type	34 AWG
Length	4200 mm
Resistance	6.2 Ω
Inductance	190 μH
60 turns chip specifications	
Material	PC-ABS
Carving Dimensions	$11.5 \times 3 \times 0.5$ mm
Outer Dimensions	$53.5 \times 20 \times 1$ mm

4.4 Evaluation of SVEH

This section illustrates the frequency response and output waveform of the SVEH and determine the output voltage and power characteristics. We also apply the rectification circuit introduced in section 3.1.1 to test the SVEH output waveform and compare it to the VEH output waveform.

4.4.1 Frequency Response of the 60 Turns SVEH

A frequency-response test was utilized to evaluate the performance of the SVEH at different frequencies and resistive loads. The experimental setup, shown in Fig-

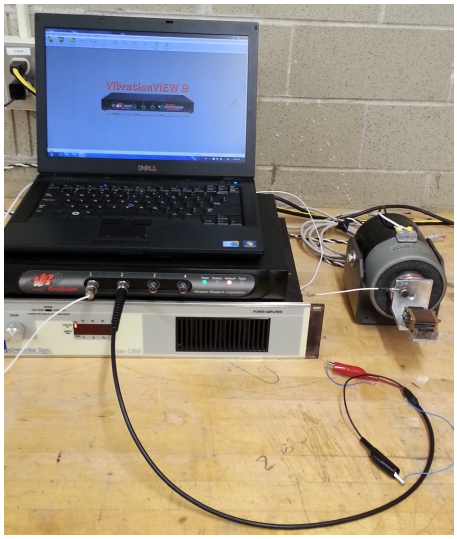

Figure 4.6: SVEH experimental setup

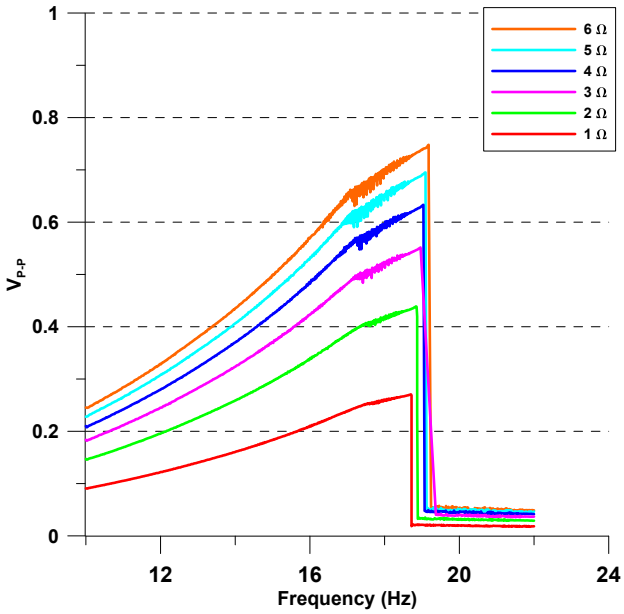

Figure 4.7: SVEH 60 turns frequency response

ure 4.6, is the same setup used for the VEH of section 2.4. The frequency sweep starts from 10 to 22 Hz at acceleration amplitude of 0.5 g. The slew rate is 1 Hz/min, therefore each sweep lasts for 12 minutes. The SVEH was aligned horizontally and the resistive loads R_L was varied from 1 to 6 Ω.

The results show an increase in output voltage from 0.270 - 0.747 V_{p-p} and bandwidth from 5.45 - 5.64 Hz when increasing the resistive load as shown in Table 4.4.

Table 4.4: Comparison between 40 and 60 turns

R_L	f_1	f_{peak}	BW	V_{peak}
1	13.60	19.24	5.64	0.747
2	13.56	19.18	5.62	0.695
3	13.53	19.14	5.61	0.630
4	13.40	18.95	5.55	0.550
5	13.36	18.90	5.54	0.350
6	13.15	18.60	5.45	0.270

We observed a frequency drop at f_{peak} where the SVEH drops from the impacting to the non-impacting branch, Figure 4.7. As the SVEH starts oscillations at low frequency (10 Hz), the mass impacts on the limiters building-up the restoring force $F(x)$. As the frequency increases the impact velocity increases and consequently the measured output voltage. The basin of attraction of the resonant (impacting) orbit shrinks as the frequency increases. Eventually the resonant branch reaches a point where the basin of safe motions disappears and the response falls down on the non-impacting branch.

4.4.2 Voltage and Power of the SVEHs

The output voltage and power of the 40-turns and 60-turns SVEHs were determined using the technique described in 2.5.3. The results show an expected increase in the 60-turns SVEH output voltage and power compared to-40 turns from 8.3 to 12.3 mW where the maximum power was calculated at $R_L = 3\,\Omega$, Figure 4.8.

The closed circuit voltage waveform at $R_L = 3\,\Omega$, Figure 4.9, indicates a higher nonlinearity compared to the cantilever VEH output waveform, Figure 2.9. This nonlinearity is a result of the seismic mass impact into the limiters. The 40 and 60 turns coil-chips output power, voltage and load R_L are listed in Table 4.5.

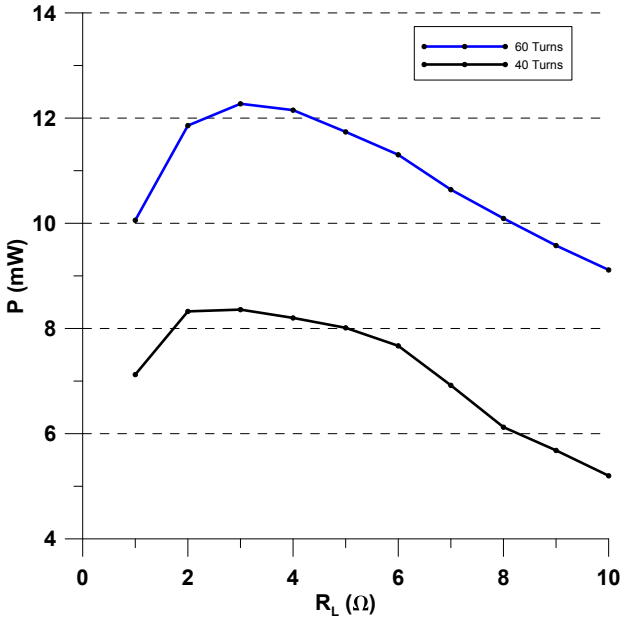

Figure 4.8: SVEHs output power

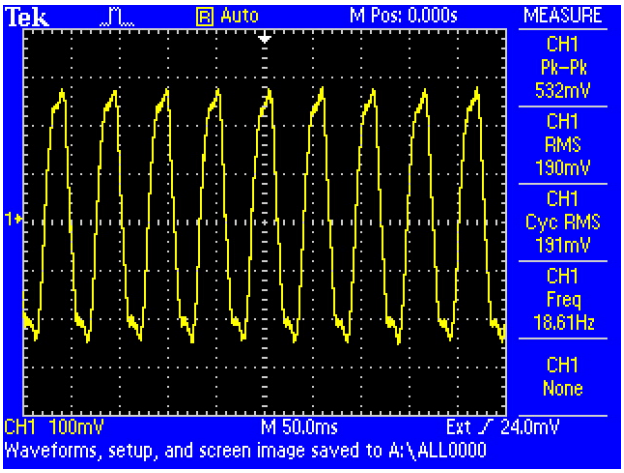

Figure 4.9: Output voltage waveform across the optimal load R_L=3 Ω for the 60-turns SVEH

4.5 Rectification Performance

We utilized the rectification circuit presented in section 3.1.1 to study its performance with the 60-turns SVEH. An open circuit test conducted to capture the output waveforms of the SVEH and the rectification circuit, as shown in Figure 4.10. These waveforms were utilized to calculate the output RMS voltages using Equation (2.16). The calculated harvester and rectified output RMS voltages are 575 mV

Table 4.5: Comparison between 40 and 60 turns

	40 turns		**60 turns**	
Load Ω	Voltage (mV)	Power (mW)	Voltage (mV)	Power (mW)
1	84.40	7.12	100.29	10.06
2	129.10	8.33	155.61	11.86
3	158.40	8.36	191.88	12.27
4	181.30	8.20	220.47	12.15
5	200.10	8.01	242.30	11.74
6	214.50	7.67	260.42	11.30
7	220.10	6.92	272.91	10.64
8	221.20	6.12	284.16	10.09
9	226.00	5.68	293.59	9.58
10	228.00	5.20	301.89	9.11

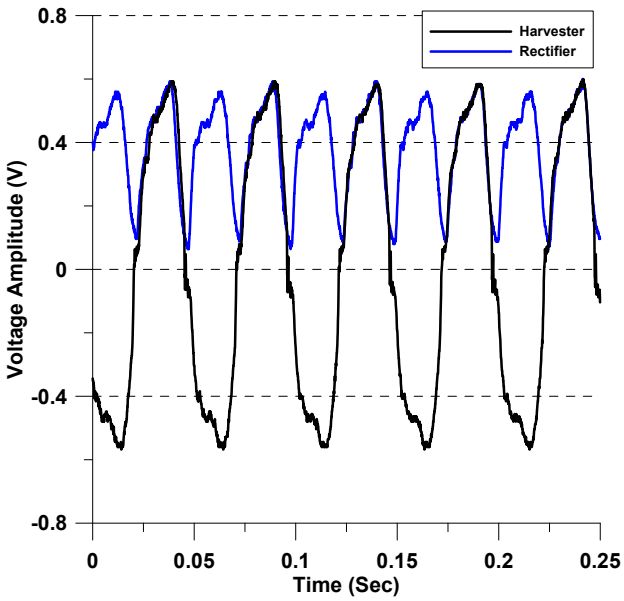

Figure 4.10: SVEH output voltage waveform

and 535 mV, respectively. These calculations indicate a 93 % voltage efficiency at open circuit; in comparison to 97 % VEH-rectifier voltage efficiency at optimal load (see subsection 3.2). Moreover, the SVEH higher nonlinearity did not significantly effect the AC/DC converted waveform.

We also tested the rectifier at close circuit SVEH ($R_L = 3\,\Omega$), shown in Figure 4.9, where the SVEH provides an output RMS voltage of 191.88 mV. The result

indicated that the rectification circuit was operating in the sub-threshold region (weak-inversion region) because of the threshold voltage V_{th} applied to the MOSFETs is $< 400\,\text{mV}$ [63].

4.6 Summary

This chapter introduced and analyzed the performance of the springless vibration energy harvester (SVEH) using different coil-chips. The polycarbonate coil-chip and the re-designed PC-ABS coil-chip specifications were compared and listed. In addition, the specifications of the 25, 40 and 60-tuns SVEHs were compared and listed.

Experiments present the 60-turns SVEH frequency-response curves in the range of 10 to 22 Hz at different loads ($R_L = 1$–$6\,\Omega$). Output voltage and power analysis were carried out at the peak point to compare the performance of the 40 and 60-turns SVEHs at different loads (1–10 Ω). The determined output RMS voltage and power of the 40-turns SVEH at optimal load $R_L = 3\,\Omega$ are 134.68 mV and 8.36 mW. On the other hand, at 60-turns SVEH output voltage and power increased to 191.88 mV and 12.27 mW at optimal load $R_L = 3\,\Omega$. The SVEH-rectifier circuit analysis shows an open circuit voltage efficiency of 93 %. However, the power efficiency at closed circuit was zero because no current can pass through the rectifier due to the lower threshold voltage $V_{th} < 400\,\text{mV}$.

Chapter 5

Conclusions and Future Work

5.1 Conclusions

We re-designed and experimentally studied two architectures of vibration energy harvesting, the cantilever (VEH) and the springless (SVEH). Voltage and power frequency responses have been analyzed to examine the response as a function of resistive loads R_L. The same experimental setup has been used in all tests to keep the consistency of the results. An acceleration amplitude of 0.5 g and sweep rate of 1 Hz/min have been utilized in all tests. The frequency range in each case varies depending on the VEH operating frequency. The cantilever VEH operates in the frequency range of 57–59 Hz. The SVEH operates in the frequency range of 13–18 Hz. The VEHs have been re-designed by developing a 3D printed coil-chip to carry more coil turns in order to increase the output voltage. The VEH 3D coil-chip can hold up to 80-turns resulted in increasing the output power at the peak frequency and an optimal load of $R_L = 40\,\Omega$, from 6.1 mW to 14.3 mW compared to the 30-turns coil-chip. The SVEH has been re-designed to have 60-turns coil-chip which also increased the output revert power at optimal load of $R_L = 3\,\Omega$ from 8.36 mW to 12.27 mW compared to the 40-turns coil-chip.

We introduced a passive rectification circuit and a smoothing capacitor to manage the VEHs output. We utilized different approaches to measure the output voltage, power, and efficiency. The cantilever VEH output waveform was analyzed

in three stages: harvester, rectifier only, and rectifier with a smoothing capacitor, as a function of different resistive loads R_L. The passive rectifier converts the harvester AC signal into a DC signal with a voltage efficiency of 97 % and power efficiency of 95 % at an optimal load of 40 Ω. Smoothing capacitors of 220 μF and 1000 μF were introduced to minimize the rectifier output waveform ripples. The smoothing capacitor trades-in minimized ripples with output power efficiency resulting in input-output power efficiency η_P of 79.45 % using 220 μF and 84.33 % using 1000 μF at an optimal load of 55 Ω. We were not able to rectify the SVEH waveform since it had low output voltage (191.88 mV) at an optimal load of $R_L = 3\,\Omega$ while the rectifier requires at least $V_{th} = 400$ mV threshold voltage to operate the switching MOSFETs. However, the passive rectifier had been tested with the open circuit SVEH, resulting in a rectified output signal with a voltage efficiency of 93 %.

We developed an electromechanical model for the cantilever VEH. The coupled model was solved numerically and analytically using the experiential data and the identified parameters to determine the quality factors, frequency response, output voltage and power as a function of resistive load R_L. Then, we compare the results to the experimental data and calculated the average errors in percentage.

Parameter identification techniques were utilized to determine the natural frequency ω_n, the mechanical quality factor Q_m, the total quality factor Q_t and the effective average magnetic field density B of the cantilever VEH using the obtained experimental data. The natural frequency $\omega_n = 57.85$ Hz was calculated using the backbone technique. The quality factors were estimated using Equation (3.8). The effective average magnetic field density B was determined using the total and mechanical quality factors.

5.2 Future Work

The electromagnetic VEHs showed auspicious results in terms of voltage and power make them usable candidates to power up some electronics applications. We can introduce other transduction techniques and combine them with the electromag-

netic technique in a new state-of-art design. The miniaturization application is an attractive approach, where we can utilize the MEMS technology to fabricate a small scale cantilever VEH or SVEH in consideration with the device parameters.

Also, we can develop the mechanical and electrical model by introducing the non-linearity term for the cantilever VEH. Finally, We may present a better rectification model by including the MOSFETs ON and OFF states.

References

[1] M Soliman, E Abdel-Rahman, E El-Saadany, and R Mansour. A Wideband Vibration-based Energy Harvester. *Journal of Micromechanics and Microengineering*, 18(11):115021, 2008.

[2] M Ibrahim. Design, Modeling, and Fabrication of a Hybrid Energy Harvester. Master's thesis, University of Waterloo, 2014.

[3] I Khodadad, L Ball, R Bhagat, I Shafieloo, E Abdel-rahman, E El-saadany, R Mansour, and A Hajian. Optimization of a Micro Power Unit. *ASME Computers and Information in Engineering Conference*, 2011.

[4] A Kempitiya, D Tasciuc, and M Hella. Analysis and Otimization of Asynchronously Controlled Electrostatic Energy Harvesters. *IEEE Transactions on Industrial Electronics*, 59(1):456–463, 2012.

[5] M Green. *Third Generation Photovoltaics Advanced Solar Energy Conversions*. Springer, 2006.

[6] J Thomas, M A Qidwai, and J C Kellogg. Energy Scavenging for Small-scale Unmanned Systems. *Journal of Power Sources*, 159(2):1494–1509, 2006.

[7] D Brunelli, C Moser, L Thiele, and L Benini. Design of a Solar Harvesting Circuit for Battery-less Embedded Systems. *IEEE Transactions on Circuits and Systems*, 56:2519–2528, 2009.

[8] B I Ismail and W H Ahmed. Thermoelectric Power Generation Using Waste-

Heat Energy as an Alternative Green Technology. *Electrical Engineeringe EENG*, pages 27–39, 2009.

[9] R Vullers, R Schaijk, I Doms, C Hoof, and R Mertens. Micropower energy harvesting. *Solid-State Electronics*, 53(7):684–693, 2009.

[10] J Gilbert and F Balouchi. Comparison of Energy Harvesting Systems for Wireless Sensor Networks. *International Journal of Automation and Computing*, 5(4):334–347, 2008.

[11] J Zhang, Y Huang, and P Cao. Harvesting RF Energy with Rectenna Arrays. *6th European Conference on Antennas and Propagation (EUCAP)*, pages 365–367, 2012.

[12] J Zhang, Y Huang, and P Cao. An Investigation of Wideband Rectennas for Wireless Energy Harvesting. *Wireless Engineering and Technology*, pages 107–116, 2014.

[13] M Yilmaz. Passive Full-Wave MOSFET Rectifiers for Electromagnetic Harvesting. Master's thesis, University of Waterloo, 2013.

[14] K Elrayes. Low-Frequency Electromagnetic Energy Harvesting. Master's thesis, University of Waterloo, 2011.

[15] S Meninger, J Mur-Miranda, R Amirtharajah, A Chandrakasan, and J H Lang. Vibration-to-electric energy conversion. *IEEE Transactions on Very Large Scale Integration (VLSI)Systems*, 9(1):64–76, 2001.

[16] K Tao, J Miao, S Lye, and X Hu. Sandwich-structured Two-dimensional MEMS Electret Power Generator for Low-level Ambient Vibrational Energy Harvesting. *Sensors and Actuators A: Physical*, 228:95–103, 2015.

[17] K Tao, S Liu, S Lye, J Miao, and X Hu. A Three-dimensional Electret-based Micro Power Generator for Low-level Ambient Vibrational Energy Harvesting. *Journal of Micromechanics and Microengineering*, 24(6):065022, 2014.

[18] Y Naruse, N Matsubara, K Mabuchi, M Izumi, and K Honma. Electrostatic micro power generation from low-frequency vibration such as human motion. *Journal of Micromechanics and Microengineering*, 19(9):094002, 2009.

[19] E Aktakka. A Micro Inertial Energy Harvesting Platform With Self-supplied Power Management Circuit for Autonomous Wireless Sensor Nodes. *IEEE Journal of Solid-State Circuits*, 49(9):2017–2029, 2014.

[20] F Cottone. Introduction to Vibration energy harvesting. NiPS Energy Harvesting Summer School, 2011.

[21] B Joyce. Development of An Electromagnetic Energy Harvester for Monitoring Wind Turbine Blades Development of an Electromagnetic Energy Harvester for Monitoring Wind Turbine Blades. Master's thesis, Virginia Polytechnic Institute and State University, 2011.

[22] A Khaligh, P Zeng, and C Zheng. Kinetic Energy Harvesting Using Piezoelectric and Electromagnetic Technologies. *IEEE Transactions on Industrial Electronics*, 57(3):850–860, 2010.

[23] C Dagdevirena, B Yang, Y Su, P Trand, P Joea, E Andersona, J Xiab, V Doraiswamyd, B Dehdashtie, X Fengf, B Lub, R Postone, Z Khalpeye, R Ghaffarig, Y Huangc, M Slepiand, and J Rogersa. Conformal Piezoelectric Energy Harvesting and Storage From Motions of The Heart, Lung, and Diaphragm. *Proceedings of the National Academy of Sciences PNAS*, 111(5):1927–32, 2014.

[24] N S Shenck and J A Paradiso. Energy Scavenging With Shoe-Mounted Piezoelectric. *IEEE Micro*, pages 30–42, 2001.

[25] D Han and K Yun. Piezoelectric Energy Harvester Using Mechanical Frequency Up Conversion For Operation at Low-level Accelerations and Low-frequency Vibration. *Microsystem Technologies*, 21(8):1669–1676, 2014.

[26] M Halim and J Park. A Non-resonant Frequency Up-converted Electromagnetic Energy Harvester From Human Body Induced Vibration for Hand-held Smart System Applications. *Journal of Applied Physics*, 115(9), 2014.

[27] A Harouna, I Yamadac, and S Warisawa. Micro Electromagnetic Vibration Energy Harvester Based on Free Impact Motion for Low Frequency Large Amplitude Operation. *Sensors and Actuators A: Physical*, pages 87–98, 2015.

[28] Y Choi, S Ju, S H Chae, S Jun, and C Ji. Low-frequency Vibration Energy Harvester Using a Spherical Permanent Magnet With Controlled Mass Distribution. *Smart Materials and Structures*, 24(6):065029, 2015.

[29] G Szarka, S Burrow, P Proynov, and B Stark. Maximum Power Transfer Tracking for Ultralow-Power Electromagnetic Energy Harvesters. *IEEE Transactions on Power Electronics*, 29(1):201–212, 2014.

[30] V Vijayan and K Vinida. A Review of AC-DC Boost Converters for Low Voltage Energy Harvesting. 4(6):841–846, 2014.

[31] R Tiwari, K Ryoo, A Schlichting, and E Garcia. Extremely low-loss rectification methodology for low-power vibration energy harvesters. *Smart Materials and Structures*, 22(6), 2013.

[32] M H Rashid. *Power Electronics Handbook*. Academic Press, 2001.

[33] https://www.docstoc.com/docs/127650863/Half-Wave-Rectier-Theory

[34] X Wang, X Liang, and H Wei. A Study of Electromagnetic Vibration Energy Harvesters with Different Interface Circuits. *Mechanical Systems and Signal Processing*, 58-59:376–398, 2015.

[35] http://forum.allaboutcircuits.com/showthread.php?t=56064

[36] M I Younis. *MEMS Linear and Nonlinear Statics and Dynamics*. Springer, 2011.

[37] K Ogata. System Dynamics. Prentice Hall, 4 edition, 2004

[38] M Bendame, E Abdel-Rahman, and M Soliman. Test and Validation of a Nonlinear Electromagnetic Energy Harvester. *International Conference on Micro and Nano systems*, 4, 2014.

[39] S Beeby, M Tudor, R Torah, E Koukharenko, S Roberts, T O'Donnell, and S Roy. Macro and Micro Scale Electromagnetic Kinetic Energy Harvesting Generators. *Journal of Microsystem technology*, pages 26–28, 2006.

[40] https://www.trifield.com/content/dc-gaussmeter-model-gm2/

[41] https://uwaterloo.ca/3d-print-centre/3d/making-print/3d-print-cost

[42] http://www.labworks-inc.com/downloads

[43] http://www.vibrationresearch.com/VR9500.html

[44] http://72.34.224.196/Model-3055B3-General-Purpose-Accelerometer-P2187.aspx

[45] http://www.tek.com/datasheet/mso2000-dpo2000/mso2000b-series-dpo2000b-series-datasheet

[46] http://www.keysight.com/en/pd-1896657-pn-U1272A

[47] A Cammarano, S Neild, S Burrow, and D Inman. The Bandwidth of Optimized Nonlinear Vibration-based Energy Harvesters. *Smart Materials and Structures*, 23(5), 2014.

[48] C Peters, J Handwerker, D Maurath, and Y Manoli. A Sub-500 mV Highly Efficient Active Rectifier for Energy Harvesting Applications. *IEEE Transactions on Circuits and Systems I: Regular Papers*, 58(7):1542–1550, 2011.

[49] http://www.vishay.com/docs/68741/si2301cd.pdf

[50] http://www.onsemi.com/pub_link/Collateral/NTJS3157N-D.PDF

[51] D Irwin. *The Industrial Electronics Handbook*. CRC Press, 1 edition, 1997.

[52] N G Elvin and A A Elvin. An Experimentally Validated Electromagnetic Energy Harvester. *Journal of Sound and Vibration*, 330(10):2314–2324, 2011.

[53] L Wang, T Kazmierski, B Al-Hashimi, S Beeby and R Torah. Integrated approach to energy harvester mixed technology modelling and performance optimisation. *EDAA*, 2008.

[54] D Zill. *A First Course in Differential Equations*. Cengage Learning. Inc., 5 edition, 2008.

[55] A Nayfeh and D Mook. *Nonlinear oscillations*. Wiley, 1995.

[56] D Inman. *Engineering Vibration*, volume 3. Prentice Hall, 4 edition, 2001.

[57] W Davis. Measuring Quality Factor From a Nonlinear Frequency Response With Jump Discontinuities. *Journal of Microelectromechanical Systems*, 20(4):968–975, 2011.

[58] S Beeby, M Tudor, and N White. Energy Harvesting Vibration Sources for Microsystems Applications. *Measurement Science and Technology*, 2006.

[59] C Montoro, M Schneider. *MOSFET Modeling for Circuit Analysis and Design*. World Scientific, 2007.

[60] D J Inman. Vibration and Control. Wiley, 2006.

[61] P D Mitcheson, T C Green, E M Yeatman, and A S Holmes. Architectures For Vibration Driven Micropower Generators. *Journal of Microelectromechanic System*, 13(3):429–440, 2004.

[62] M Bendame. *Springless Electromagnetic Vibration Energy Harvesters*. PhD thesis, University of Waterloo, 2015.

[63] J Fernandes, M Martins, and M Piedade. An Energy Harvesting Circuit for Self-powered Sensors. *Mixed Design of Integrated Circuits and Systems (MIXDES)*, pages 2–5, 2010.

APPENDIX A

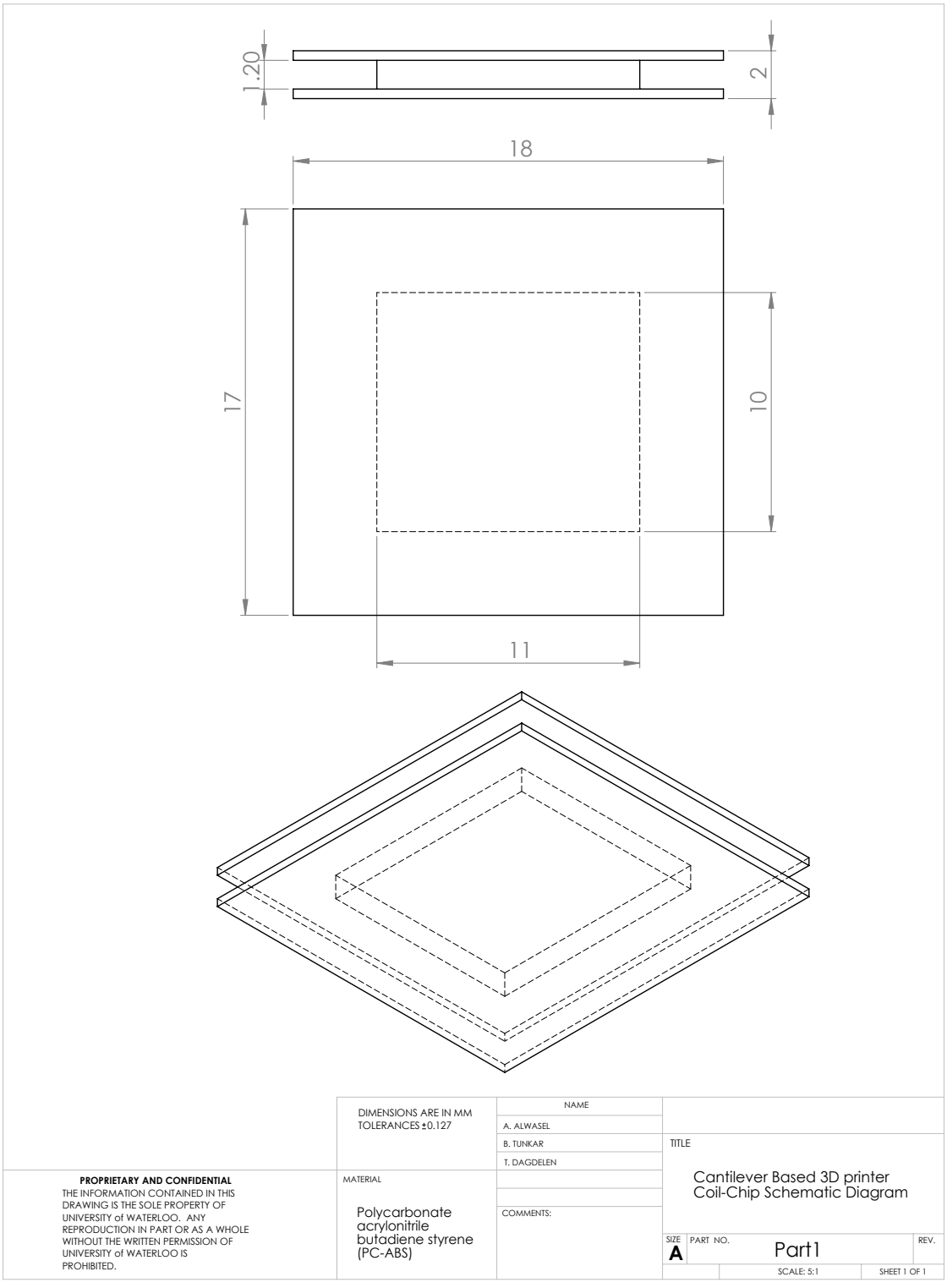

Figure 1: Blue print of the VEH coil-chip

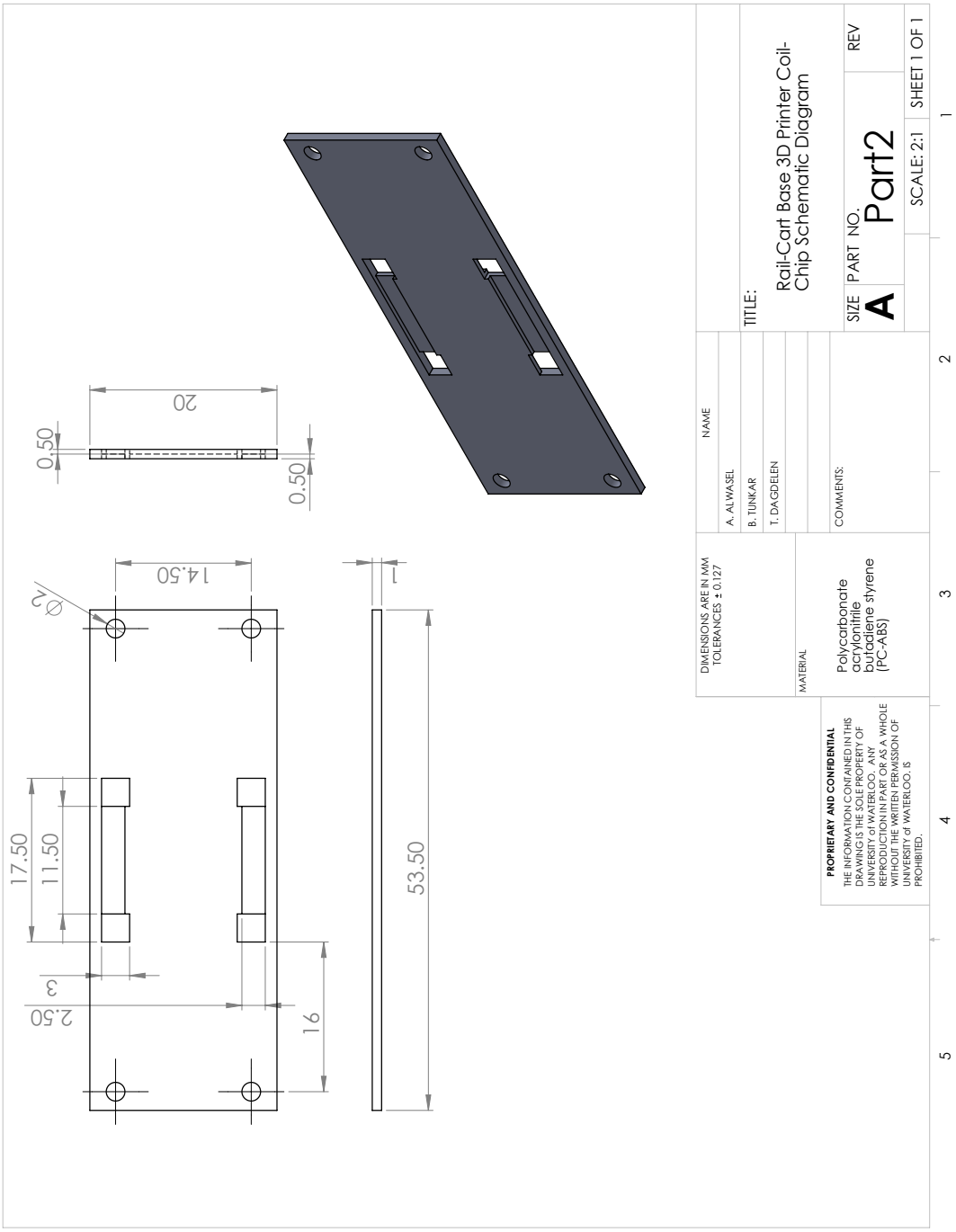

Figure 2: Blue print of the SVEH coil-chip

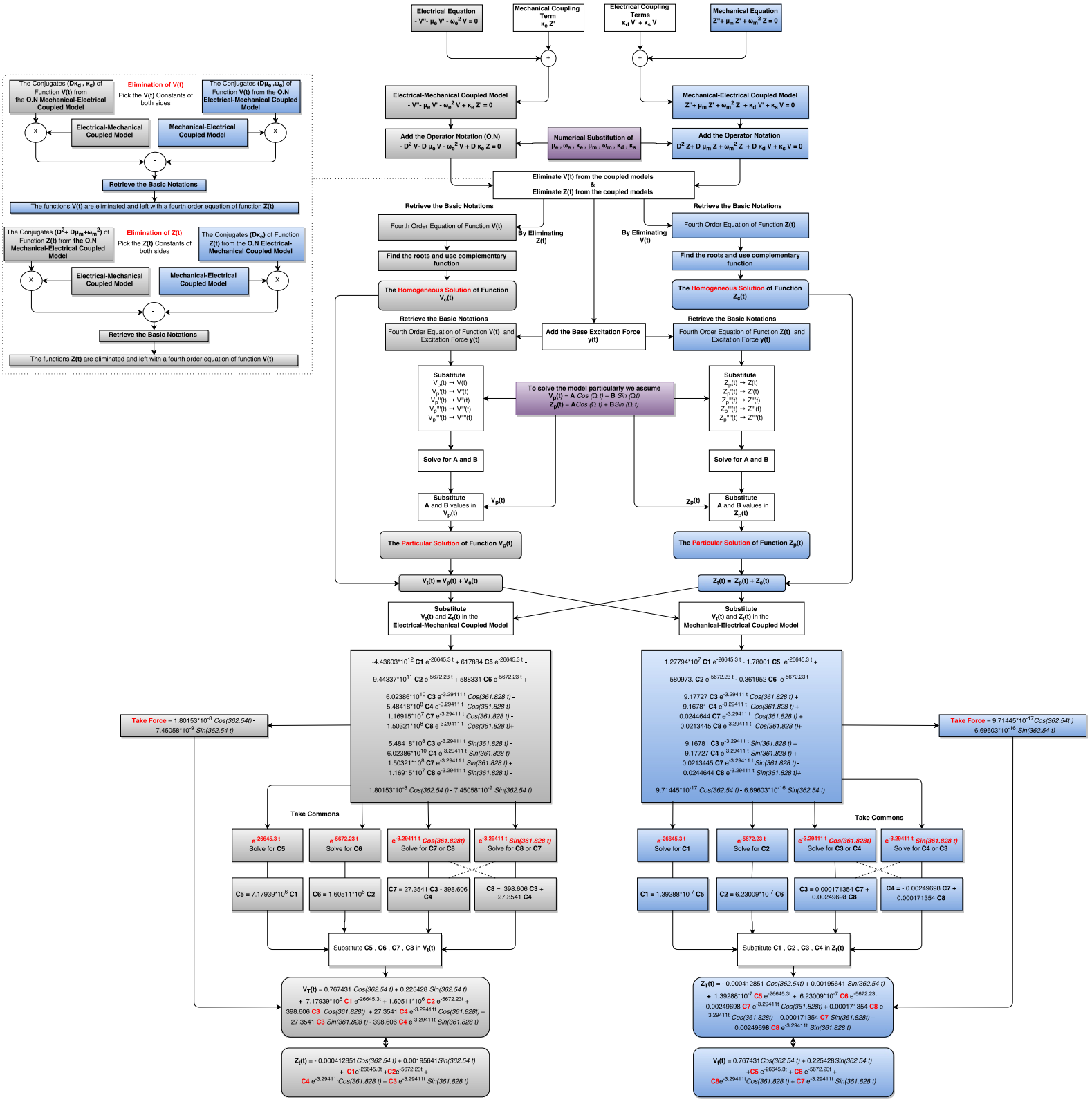

Figure 3: Operator notation linear solution